A FINITE ELEMENT METHOD FOR A NON-NEWTONIAN DILUTE POLYMER FLUID

BEN S. ASHBY, GABRIEL R. BARRENECHEA, ALEX LUKYANOV, TRISTAN PRYER, AND ALEX TRENAM

ABSTRACT. We study the discretisation of a uniaxial (rank-one) reduction of the Oldroyd-B model for dilute polymer solutions, in which the conformation tensor is represented as $\sigma = b \otimes b$. Building on structural analogies with MHD, we formulate a finite element framework compatible with the de Rham complex, so that the discrete velocity is exactly divergence-free. The spatial discretisation combines an interior-penalty treatment of viscosity with upwind transport to control stress layers and we prove inf-sup conditions on the mixed pairs. For time-stepping, we design an IMEX scheme that is linear at each step and show well-posedness of the fully discrete problem together with a discrete energy law mirroring the continuum dissipation. Numerical experiments on canonical benchmarks (lid-driven cavity, pipe-with-cavity and 4:1 planar contraction) demonstrate accuracy and robustness for moderate-to-high Weissenberg numbers, capturing sharp stress gradients and corner singularities while retaining the efficiency gains of the uniaxial model. The results indicate that de Rham-compatible discretisations coupled with energy-stable IMEX time integration provide a reliable pathway for viscoelastic computations at elevated elasticity.

1. Introduction

Viscoelastic fluids, such as polymer solutions, exhibit complex behaviours that differ significantly from those of Newtonian fluids due to the presence of long-chain molecules whose microstructure meaningfully affects macroscopic flow. Industrial examples include molten plastics and lubricants, while blood is a canonical biological example. Unlike Newtonian flows, governed solely by the Navier-Stokes equations, viscoelastic flows require an additional constitutive relation to account for polymer-induced stresses, leading to systems of partial differential or integro-differential equations [28, 8, 38]. Among many constitutive models, the Oldroyd-B model is a widely used benchmark that couples viscous and elastic responses by combining a Newtonian solvent with a Maxwell-type polymer contribution [22, 28]. Despite its simplicity, Oldroyd-B captures key aspects of viscoelastic behaviour and remains central in computational rheology [23, 11]. Flow regimes are commonly organised by the Weissenberg and Deborah numbers, the Weissenberg number Wi quantifies the significance of nonlinear normal-stress effects [20, 40], whereas the Deborah number De measures the dominance of elastic over viscous timescales [8]. At low De one recovers nearly Newtonian behaviour, whereas at high Wi purely elastic phenomena, including elastic turbulence and flow-induced instabilities, can appear and complicate both analysis and computation [39].

A central numerical difficulty is the *high Weissenberg number problem* (HWNP). As Wi increases, steep stress gradients and exponential boundary layers form, which frequently trigger loss of convergence or spurious oscillations [41]. The Oldroyd-B model also features unbounded extensional viscosity, further exacerbating instability [28]. Writing the constitutive law

(1.1)
$$\frac{\partial \boldsymbol{\sigma}}{\partial t} + (\boldsymbol{u} \cdot \nabla) \boldsymbol{\sigma} - (\nabla \boldsymbol{u}) \boldsymbol{\sigma} - \boldsymbol{\sigma} (\nabla \boldsymbol{u})^T = -\frac{1}{\text{Wi}} (\boldsymbol{\sigma} - \boldsymbol{I})$$

as an ODE along characteristics induced by the deformation gradient clarifies the mechanism by which eigenvalues of σ can grow and precipitate numerical breakdown [5]. This combination of physical stiffness and geometric transport underlies the need for structure-preserving discretisations.

This work introduces a finite element framework that addresses the computational challenges above by combining a model reduction with compatible spatial discretisation and energy-stable time integration. The starting point is a uniaxial (rank-one) reduction of Oldroyd-B, originally proposed in [24], in which the conformation tensor is approximated by a dyad, thereby retaining dominant alignment and stretch at reduced cost in multiple dimensions. Inspired by magnetohydrodynamics (MHD), we develop finite element methods

Date: November 26, 2025.

1

that respect the de Rham complex: velocity and pressure are approximated in $H(\operatorname{div};\Omega)$ - and L^2 -conforming spaces to enforce incompressibility exactly at the discrete level, while the polymeric vector field is placed in an $H(\operatorname{curl};\Omega)$ -conforming space to mirror the transport-rotation structure. We establish well-posedness of the and discrete energy laws mirroring the continuum dissipation for both the semi- and fully-discrete schemes. Numerical experiments on demanding benchmarks, including lid-driven cavity, pipe-with-cavity and planar contraction flows, confirm robustness at high Wi and demonstrate improved computational efficiency relative to traditional approaches.

The HWNP has been recognised since early computational rheology studies [19, 33, 10, 37], where steady solutions in benchmark problems (e.g. contractions and expansions) often failed at modest Wi. Subsequent developments pursued two complementary directions, stabilising formulations and structure-preserving discretisations. On the formulation side, the log-conformation representation [22, 23] guarantees positive-definiteness of the conformation tensor and dramatically extends attainable Wi; square-root and hyperbolic-tangent mappings provide related positivity-preserving transforms [35, 32], with comparative assessments reported in [42]. Classical stabilisations for advective transport, including SUPG/Petrov-Galerkin ideas [30] and DEVSS-type splittings [25], have also been employed, as have finite-volume and DG variants tailored to high Péclet transport of stress [18, 16]. On the structural side, energy and entropy estimates for Oldroyd-B and related models [35, 29, 34, 6] have motivated schemes that ensure discrete free-energy decay [11, 12]. Our IMEX formulation inherits a discrete energy law without resorting to fully nonlinear solves at each time step, complementing implicit log-conformation approaches [31].

Compatibility of mixed spaces plays a central role in incompressible and multiphysics flows. Finite element exterior calculus (FEEC) provides a unifying perspective on stable discretisation through commuting projections on the de Rham complex [2]. For incompressible flow and MHD, H(div)-conforming velocities and H(curl)-conforming fields improve stability and preserve differential constraints discretely [9, 36]. Our use of $H(\text{div})/L^2$ for velocity-pressure eliminates spurious pressure modes and provides exact enforcement of the divergence constraint, while the H(curl) discretisation for the polymeric vector field emulates the curl-advection structure that appears in both viscoelastic transport and MHD analogies [18]. From the algorithmic viewpoint, IMEX time integrators [4] are natural for stiff transport-relaxation systems; here we show that, coupled with the skew-symmetric treatment of convection and appropriate upwinding, they yield a discrete energy decay consistent with the continuum law.

Reduced-order modelling aims to alleviate the high computational burden of fully resolved viscoelastic simulations. Proper orthogonal decomposition (POD) and Galerkin reduced models have been explored for viscoelastic turbulence and complex flows [14], often combined with regularisation or stabilisation [15]. At the model level, rank-limited (e.g. rank-one) approximations of the conformation tensor provide a physics-based reduction that captures dominant alignment and stretch while preserving key couplings [24]. Our framework integrates such a uniaxial reduction with compatible discretisation and energy stability, thereby achieving substantial efficiency gains without sacrificing robustness.

Finally, the analogy between viscoelastic constitutive dynamics and magnetic induction in MHD provides conceptual and practical guidance. Ogilvie and Proctor [36] formalised correspondences between Oldroyd-B and MHD, including instability analogues, which motivate the enforcement of structure-preserving constraints (e.g. divergence-like and positivity conditions) and the use of H(div)/H(curl) spaces. Empirically, viscoelastic instabilities in cavity and contraction flows [40, 39, 18, 37] align with this viewpoint, and numerical treatments developed in MHD inform our stabilisation and discretisation choices.

Section 2 presents the governing equations, notation and basic assumptions. Section 3 introduces the uniaxial reduction, discusses its modelling implications and establishes key properties, including the relation to the continuum energy law. Section 4 develops the weak formulation, identifies the bilinear and trilinear forms used in discretisation and records identities needed for stability. Section 5 details the finite element spaces, their de Rham compatibility and stabilised discrete operators, and proves the relevant inf-sup conditions together with existence for the stationary problem. Section 6 presents the IMEX scheme and proves uniqueness per time step together with the discrete energy law. Section 7 reports numerical experiments for lid-driven cavity, pipe-with-cavity and 4:1 planar contraction flows. Section 8 summarises conclusions and outlines future directions.

2. Model Formulation and Preliminaries

In this section we fix notation, record the functional setting, and state standing assumptions for the analysis to follow. Throughout, $\Omega \subset \mathbb{R}^3$ denotes a bounded Lipschitz domain with boundary $\partial\Omega$ and outward unit normal \boldsymbol{n} .

We write $L^p(\omega)$ for the Lebesgue space on a measurable subset $\omega \subset \mathbb{R}^d$, $d=1,2,3, 1 \leq p \leq \infty$, with norm $\|\cdot\|_{L^p(\omega)}$. For p=2 we use the inner product $\langle\cdot,\cdot\rangle_{\omega}$ on $L^2(\omega)$ and define

$$L_0^2(\omega) := \{ q \in L^2(\omega) : \langle q, 1 \rangle_{\omega} = 0 \}.$$

When $\omega = \Omega$ we suppress the subscript and write $\langle \cdot, \cdot \rangle = \langle \cdot, \cdot \rangle_{\Omega}$.

For a nonnegative integer k, the Sobolev space $H^k(\omega)$ is defined as

(2.1)
$$H^{k}(\omega) := \{ \phi \in L^{2}(\omega) : D^{\alpha}\phi \in L^{2}(\omega) \text{ for all } |\alpha| < k \},$$

where $\alpha = (\alpha_1, \dots, \alpha_d)$ is a multi-index, D^{α} the associated weak derivative, and $|\alpha| = \sum_{i=1}^d \alpha_i$. We equip $H^k(\omega)$ with the norm and seminorm

(2.2)
$$||u||_{\mathcal{H}^{k}(\omega)}^{2} := \sum_{|\alpha| < k} ||D^{\alpha}u||_{\mathcal{L}^{2}(\omega)}^{2}, \qquad |u|_{k}^{2} := \sum_{|\alpha| = k} ||D^{\alpha}u||_{\mathcal{L}^{2}(\omega)}^{2}.$$

In particular

(2.3)
$$H_0^1(\Omega) := \{ \phi \in H^1(\Omega) : \phi |_{\partial \Omega} = 0 \}.$$

Vector- and tensor-valued fields are understood componentwise. For a scalar field $u : \mathbb{R}^d \to \mathbb{R}$, ∇u denotes the gradient column vector; for a vector field $\mathbf{v} : \mathbb{R}^d \to \mathbb{R}^d$, div \mathbf{v} is the scalar divergence and $\nabla \mathbf{v}$ the Jacobian matrix with entries $(\nabla \mathbf{v})_{ij} = \mathbf{D}_j v_i$. The Laplacian is $\Delta u := \operatorname{div}(\nabla u)$, applied componentwise to vectors. We employ the Frobenius inner product $A : B := \sum_{i,j} A_{ij} B_{ij}$ for matrices, and the associated norm $\|A\|_{\mathbf{F}}^2 := A : A$. The curl of a vector field is denoted by $\operatorname{curl} \mathbf{v}$.

For fields with divergence or curl in L² we use the standard Sobolev spaces

$$(2.4) \quad \operatorname{H}(\operatorname{div};\Omega) := \{ \phi \in [\operatorname{L}^{2}(\Omega)]^{d} : \operatorname{div} \phi \in \operatorname{L}^{2}(\Omega) \}, \qquad \operatorname{H}(\operatorname{curl};\Omega) := \{ \phi \in [\operatorname{L}^{2}(\Omega)]^{d} : \operatorname{curl} \phi \in [\operatorname{L}^{2}(\Omega)]^{d} \}.$$

These spaces will host the discrete velocity (in $H(div; \Omega)$) and the polymeric vector field (in $H(curl; \Omega)$), respectively, so as to reflect the underlying differential constraints.

Time-dependent problems are posed on [0,T] with T>0. For a Banach space X, the Bochner space $L^2(0,T;X)$ is

(2.5)
$$\mathrm{L}^2(0,T;X) := \big\{ u : [0,T] \to X \text{ strongly measurable} : \int_0^T \|u(t)\|_X^2 \mathrm{d}t < \infty \big\}.$$

When needed we also employ $H^1(0,T;X^*)$ for time derivatives in a dual space. We write $\|u\|_{\mathrm{L}^2(0,T;X)}^2 := \int_0^T \|u(t)\|_X^2 \mathrm{d}t$ and, when $X = \mathrm{H}^k(\Omega)$, abbreviate $\mathrm{L}^2(0,T;\mathrm{H}^k)$.

Unless stated otherwise, all equalities and inequalities are to be understood almost everywhere, and

Unless stated otherwise, all equalities and inequalities are to be understood almost everywhere, and constants denoted by C may change from line to line but are independent of the mesh parameters introduced later.

3. Model Description and Uniaxial Reduction

In this section we formulate the governing equations for viscoelastic fluid flow under the Oldroyd–B model and derive a reduced uniaxial model. Let $\boldsymbol{u}:\Omega\times[0,T]\to\mathbb{R}^d$ represent the velocity field of an incompressible fluid in a domain $\Omega\subset\mathbb{R}^d$ with polyhedral boundary, and let $p:\Omega\times[0,T]\to\mathbb{R}$ denote the pressure. The viscoelastic effects are captured by the symmetric conformation tensor $\boldsymbol{\sigma}:\Omega\times[0,T]\to\mathbb{R}^{d\times d}$, describing the non-Newtonian contribution to the stress.

The governing equations consist of the incompressible Navier-Stokes equations coupled with a hyperbolic constitutive law for the evolution of the conformation tensor. The Navier-Stokes equations for the velocity

and pressure are

(3.1)
$$\operatorname{Re}\left(\frac{\partial \boldsymbol{u}}{\partial t} + (\boldsymbol{u} \cdot \nabla)\boldsymbol{u}\right) = -\nabla p + 2\beta \operatorname{div}(\boldsymbol{\varepsilon}(\boldsymbol{u})) + \frac{1-\beta}{\operatorname{Wi}} \operatorname{div} \boldsymbol{\sigma},$$
$$\operatorname{div} \boldsymbol{u} = 0,$$
$$\boldsymbol{u}|_{\partial\Omega} = \boldsymbol{0},$$

where the rate-of-strain tensor $\varepsilon(u)$ is defined as

(3.2)
$$\varepsilon(\boldsymbol{u}) = \frac{\nabla \boldsymbol{u} + (\nabla \boldsymbol{u})^T}{2}.$$

The conformation tensor σ evolves according to the Oldroyd–B constitutive law

(3.3)
$$\frac{\partial \boldsymbol{\sigma}}{\partial t} + (\boldsymbol{u} \cdot \nabla) \boldsymbol{\sigma} - (\nabla \boldsymbol{u}) \boldsymbol{\sigma} - \boldsymbol{\sigma} (\nabla \boldsymbol{u})^T = -\frac{1}{\text{Wi}} (\boldsymbol{\sigma} - \boldsymbol{I}),$$

where I is the identity tensor.

The dimensionless parameters in the equations are the Reynolds number, the Weissenberg number and the elasticity ratio. The Reynolds number $\mathrm{Re} = \frac{\rho U L}{\eta}$ is the ratio of inertial to viscous forces, where ρ is the fluid density, U a characteristic velocity, L a characteristic length and η the dynamic viscosity. The Weissenberg number $\mathrm{Wi} = \frac{\lambda U}{L}$ represents the ratio of the characteristic polymer relaxation time λ to the flow timescale L/U. The elasticity ratio $\beta = \frac{\eta_s}{\eta}$ is the ratio of the solvent viscosity η_s to the total viscosity $\eta = \eta_s + \eta_p$, where η_p is the polymer contribution to the viscosity. These parameters characterise the relative importance of inertial, viscous and elastic effects in viscoelastic flows and govern the dynamic behaviour of the system.

3.1. **Remark** (Boundary and initial conditions). Throughout this work we assume no-slip boundary conditions for the velocity field u, so that u = 0 on $\partial\Omega$. Under this assumption there is no inflow boundary for the conformation tensor σ , and no explicit boundary conditions are required for σ .

In situations where the velocity boundary conditions are not trivial, for example when Dirichlet data prescribe a non-zero velocity u = g on a portion $\Gamma \subset \partial \Omega$, suitable boundary conditions must also be imposed for the conformation tensor. The equation (3.3) is hyperbolic in space and therefore requires boundary data only on the inflow boundary

(3.4)
$$\Gamma_{-} = \{ \boldsymbol{x} \in \Gamma : \boldsymbol{g}(\boldsymbol{x}) \cdot \boldsymbol{n}(\boldsymbol{x}) < 0 \},$$

where n is the outward unit normal to $\partial\Omega$. On Γ_{-} we prescribe the inflow conformation via

(3.5)
$$\sigma = \sigma_{\rm in} \quad \text{on } \Gamma_{-},$$

where $\sigma_{\rm in}$ is a positive-definite tensor representing the polymeric conformation entering the domain. At the initial time we set

(3.6)
$$\mathbf{u}(\mathbf{x},0) = \mathbf{u}_0(\mathbf{x}), \qquad \mathbf{\sigma}(\mathbf{x},0) = \mathbf{\sigma}_0(\mathbf{x}),$$

where u_0 is the initial velocity (assumed solenoidal and compatible with the boundary conditions) and σ_0 is a positive-definite tensor field representing the initial conformation state.

3.2. Strong-stretch regime and uniaxial reduction. As mentioned in the introduction, the analysis in [24] focuses on regimes with strongly stretched polymers and large Weissenberg number, in which the conformation tensor dominates the isotropic contribution, $\|\sigma\| \gg 1$. In this setting the relaxation term in (3.3) is approximated by

$$-\mathrm{Wi}^{-1}(\boldsymbol{\sigma} - \boldsymbol{I}) \approx -\mathrm{Wi}^{-1}\boldsymbol{\sigma},$$

so that the constitutive law is replaced by the upper-convected Maxwell-type approximation

(3.7)
$$\frac{\partial \boldsymbol{\sigma}}{\partial t} + (\boldsymbol{u} \cdot \nabla) \boldsymbol{\sigma} - (\nabla \boldsymbol{u}) \boldsymbol{\sigma} - \boldsymbol{\sigma} (\nabla \boldsymbol{u})^T = -\frac{1}{W_i} \boldsymbol{\sigma}.$$

This step changes the isotropic equilibrium from $\sigma = I$ to $\sigma = 0$, in the absence of flow the polymer stress relaxes to zero, corresponding to an effectively Newtonian response.

On top of this strong-stretch approximation we adopt a uniaxial ansatz for the conformation tensor,

$$\sigma = \mathbf{b} \otimes \mathbf{b},$$

where $\boldsymbol{b}:\Omega\times[0,T]\to\mathbb{R}^d$ is a vector field representing the primary direction and magnitude of polymeric stress, and \otimes denotes the dyadic product. Physically, \boldsymbol{b} encodes the dominant direction and magnitude of polymer chain alignment and stretching within the fluid: its magnitude reflects the extent of polymeric elongation, while its direction corresponds to the principal axis along which polymer chains are aligned by the flow.

This assumption reflects a dominant alignment of polymer molecules in the direction of b, which is a reasonable approximation in flows with strong uniaxial stretching or pronounced alignment of stress. It is particularly relevant in regimes where polymer chains predominantly align in a single direction due to flow-induced stretching, such as in extensional or high-shear flows. One of our goals is to explore, through computation, the range of applicability of this modelling assumption.

Substituting (3.8) into the constitutive equation (3.3), we rewrite the evolution of σ in terms of b. Differentiating σ with respect to time gives

$$\frac{\partial \boldsymbol{\sigma}}{\partial t} = \frac{\partial \boldsymbol{b}}{\partial t} \otimes \boldsymbol{b} + \boldsymbol{b} \otimes \frac{\partial \boldsymbol{b}}{\partial t}.$$

Similarly,

$$(\boldsymbol{u} \cdot \nabla)\boldsymbol{\sigma} = ((\boldsymbol{u} \cdot \nabla)\boldsymbol{b}) \otimes \boldsymbol{b} + \boldsymbol{b} \otimes ((\boldsymbol{u} \cdot \nabla)\boldsymbol{b}),$$

 $(\nabla \boldsymbol{u})\boldsymbol{\sigma} = ((\nabla \boldsymbol{u})\boldsymbol{b}) \otimes \boldsymbol{b},$
 $\boldsymbol{\sigma}(\nabla \boldsymbol{u})^T = \boldsymbol{b} \otimes ((\nabla \boldsymbol{u})\boldsymbol{b}).$

Each term remains a dyadic product of b with itself, so we can equate the coefficients of these products. This yields the evolution equation for b:

(3.9)
$$\frac{\partial \boldsymbol{b}}{\partial t} + (\boldsymbol{u} \cdot \nabla) \boldsymbol{b} - (\boldsymbol{b} \cdot \nabla) \boldsymbol{u} = -\frac{1}{\text{Wi}} \boldsymbol{b}.$$

The uniaxial assumption ensures that the tensor evolution remains aligned with b: the terms in (3.3) act only to modify the magnitude and orientation of b, rather than introducing additional stress directions or degrees of freedom.

3.3. Remark (Uniaxial boundary and initial conditions). As for the full system, no boundary conditions are required for b in the absence of inflow boundaries, while on inflow portions of the boundary b must be prescribed consistently with the imposed conformation.

The initial condition for \boldsymbol{b} can be derived from the initial conformation tensor $\boldsymbol{\sigma}_0$ by an eigenvalue decomposition. Since $\boldsymbol{\sigma}_{\text{in}}$ and $\boldsymbol{\sigma}_0$ are positive definite in physical flows, they are not rank-one, so an approximation is required to ensure compatibility with the reduced model. A natural choice is to retain only the dominant stress mode, extracting the largest eigenvalue λ_1 and corresponding eigenvector \boldsymbol{v}_1 so that

(3.10)
$$\sigma_0 \approx \lambda_1 v_1 \otimes v_1$$
.

The reduced variable is then defined as $\mathbf{b} = \sqrt{\lambda_1} \mathbf{v}_1$. This projection ensures that the reduced model captures the dominant stress direction while remaining consistent with the original conformation tensor.

3.4. **Remark** (The "do nothing" configurations). In the full Oldroyd–B model, the identity tensor I represents the "do nothing" configuration for the conformation tensor σ . The relaxation term $-\text{Wi}^{-1}(\sigma - I)$ ensures that σ relaxes toward this isotropic equilibrium state in the absence of external forces or flow. In eigenvalue terms, $\sigma = I$ corresponds to all eigenvalues being equal to 1, reflecting an isotropic stress state with no preferred direction.

Under the strong-stretch approximation (3.7) and the uniaxial assumption (3.8), the conformation tensor is expressed as $\sigma = b \otimes b$, where b encodes the polymeric stress direction and magnitude. This imposes a rank-one structure on σ , so σ can have at most one nonzero eigenvalue, namely $||b||^2$, and the relaxation acts towards b = 0 rather than towards $\sigma = I$. Consequently, the isotropic equilibrium state $\sigma = I$ of Oldroyd–B cannot be represented within the reduced model, whose natural "do nothing" configuration is b = 0 (hence $\sigma = 0$), corresponding to vanishing polymer stress and an effectively Newtonian response.

The uniaxial assumption reduces the dimensionality of the system. The original tensorial constitutive law requires evolving d(d+1)/2 independent components of the symmetric tensor σ , while the vector b has

only d components. This simplification is particularly advantageous in three-dimensional problems, where the number of degrees of freedom is reduced from six (for σ) to three (for b).

This reduction is not without a price, however: there is an inherent limit to the model's ability to capture secondary stress components orthogonal to b. This trade-off needs to be carefully considered in applications involving complex flow patterns or strong interactions between multiple stress components.

A further structural feature of the reduced model is that the vector field \boldsymbol{b} becomes asymptotically solenoidal, as the following result shows.

3.5. Proposition (Asymptotic solenoidal stress vector field). Let b solve (3.9) and assume that the velocity field u satisfies div u = 0. Then

(3.11)
$$\lim_{t \to \infty} \operatorname{div} \boldsymbol{b}(t, \boldsymbol{x}) = 0 \quad \text{for all } \boldsymbol{x} \in \Omega.$$

Proof Define y = div b. Taking the divergence of both sides of (3.9), and using div u = 0, we obtain

(3.12)
$$\frac{\partial y}{\partial t} + (\mathbf{u} \cdot \nabla)y = -\frac{1}{W_i}y.$$

This is a linear first-order partial differential equation for y, in which the convective term $(\boldsymbol{u} \cdot \nabla)y$ advects the divergence along fluid trajectories, and the relaxation term $-\frac{1}{W_i}y$ drives y toward zero.

Along a characteristic curve x(t) of the velocity field, satisfying $\dot{x}(t) = u(x(t), t)$, the quantity y(t, x(t))solves the ordinary differential equation

(3.13)
$$\frac{\mathrm{d}}{\mathrm{d}t}y(t, \boldsymbol{x}(t)) = -\frac{1}{\mathrm{Wi}}y(t, \boldsymbol{x}(t)),$$

with solution

(3.14)
$$y(t, \boldsymbol{x}(t)) = y(0, \boldsymbol{x}(0)) \exp\left(-\frac{t}{W_i}\right).$$

As $t \to \infty$, the exponential decay ensures that $y(t, \boldsymbol{x}(t)) \to 0$, and therefore div $\boldsymbol{b}(t, \boldsymbol{x}) \to 0$ along every trajectory, as claimed.

3.6. Remark (Relaxation in the reduced model). The proposition shows that, under the combined effects of relaxation and advection, the vector field b asymptotically approaches a divergence-free configuration. In the absence of external forcing, the polymeric stress field therefore tends toward an equilibrium state in which stress magnitudes decay over time and no net divergence is generated. This is consistent with the expectation that, in the long-time limit, the reduced model relaxes toward a stable configuration governed by the balance between advection and relaxation.

Collecting the above simplifications and assumptions, and in particular using the rank-one ansatz $\sigma = b \otimes b$ and the divergence-free constraints div u=0 and div b=0 (motivated by the discussion and Proposition above), the reduced system analysed in this work reads

(3.15)
$$\operatorname{Re}\left(\frac{\partial \boldsymbol{u}}{\partial t} + (\boldsymbol{u} \cdot \nabla)\boldsymbol{u}\right) - 2\beta\operatorname{div}(\boldsymbol{\varepsilon}(\boldsymbol{u})) + \nabla p = \frac{1-\beta}{\operatorname{Wi}}(\boldsymbol{b} \cdot \nabla)\boldsymbol{b} \quad \operatorname{in} \ \Omega \times (0,T),$$

$$\frac{\partial \boldsymbol{b}}{\partial t} + (\boldsymbol{u} \cdot \nabla)\boldsymbol{b} - (\boldsymbol{b} \cdot \nabla)\boldsymbol{u} = -\frac{1}{\operatorname{Wi}}\boldsymbol{b} \qquad \qquad \operatorname{in} \ \Omega \times (0,T),$$

$$\operatorname{div} \boldsymbol{u} = 0 \qquad \qquad \operatorname{in} \ \Omega \times (0,T),$$

$$\operatorname{div} \boldsymbol{b} = 0 \qquad \qquad \operatorname{in} \ \Omega \times (0,T),$$

$$\boldsymbol{u} = \boldsymbol{0} \qquad \qquad \operatorname{on} \ \partial \Omega \times (0,T),$$

$$\boldsymbol{u} = \boldsymbol{0} \qquad \qquad \operatorname{on} \ \partial \Omega \times (0,T),$$

$$\boldsymbol{u}(\boldsymbol{x},0) = \boldsymbol{u}_0(\boldsymbol{x}) \qquad \qquad \operatorname{in} \ \Omega \times \{0\},$$

$$\boldsymbol{b}(\boldsymbol{x},0) = \boldsymbol{b}_0(\boldsymbol{x}) \qquad \qquad \operatorname{in} \ \Omega \times \{0\},$$

Note that the upper-convected derivative of \boldsymbol{b} admits the representation

(3.16)
$$\frac{\partial \boldsymbol{b}}{\partial t} + (\boldsymbol{u} \cdot \nabla) \boldsymbol{b} - (\boldsymbol{b} \cdot \nabla) \boldsymbol{u} = \frac{\partial \boldsymbol{b}}{\partial t} - \operatorname{curl}(\boldsymbol{u} \times \boldsymbol{b}),$$

where we have used the vector identity

$$\operatorname{curl}(\boldsymbol{u} \times \boldsymbol{b}) = (\boldsymbol{b} \cdot \nabla)\boldsymbol{u} - (\boldsymbol{u} \cdot \nabla)\boldsymbol{b} + \boldsymbol{u}\operatorname{div}\boldsymbol{b} - \boldsymbol{b}\operatorname{div}\boldsymbol{u}$$

together with div $\mathbf{u} = \text{div } \mathbf{b} = 0$. In particular, the divergence-free constraints eliminate terms associated with isotropic expansion or compression of \mathbf{b} , so that only advection and shearing/stretching contribute to the evolution of \mathbf{b} .

The divergence-free property div $\mathbf{b} = 0$ is consistent with the interpretation of \mathbf{b} as the dominant direction and magnitude of polymeric stress, it indicates that there are no artificial sources or sinks of stress within the domain, and that stress is transported and redistributed by the flow without spurious accumulation.

This structure highlights a strong analogy with magnetohydrodynamics (MHD), where the magnetic field is divergence-free and its evolution contains a term $\operatorname{curl}(\boldsymbol{u}\times\boldsymbol{B})$ describing the advection and stretching of magnetic field lines by the velocity field. In the present viscoelastic setting, the term $\operatorname{curl}(\boldsymbol{u}\times\boldsymbol{b})$ plays an analogous role, capturing the advection and alignment of polymeric stress vectors. This analogy provides useful insight into the dynamics of \boldsymbol{b} and motivates the adaptation of numerical techniques from MHD to viscoelastic fluid simulations.

4. Weak Formulation

In this section we derive the weak formulation of the system described in §3. The weak formulation provides a framework suitable for numerical approximation by finite element methods.

To express the governing equations in weak form, we introduce the following bilinear and trilinear forms:

(4.1)
$$\mathcal{O}(\boldsymbol{w};\boldsymbol{u},\boldsymbol{v}) := \langle (\boldsymbol{w} \cdot \nabla)\boldsymbol{u}, \boldsymbol{v} \rangle, \\ \mathcal{A}(\boldsymbol{u},\boldsymbol{v}) := \langle \nabla \boldsymbol{u}, \nabla \boldsymbol{v} \rangle, \\ \mathcal{C}(\boldsymbol{v},q) := -\langle \operatorname{div} \boldsymbol{v}, q \rangle, \\ \mathcal{D}(\boldsymbol{c},s) := \langle \boldsymbol{c}, \nabla s \rangle.$$

Here \mathcal{O} is the trilinear convective form and \mathcal{A} is the bilinear form associated with viscous diffusion. The form \mathcal{C} couples velocity and pressure and is used to enforce the divergence-free condition for the velocity field, while \mathcal{D} couples the polymeric vector field to a scalar multiplier and will be used to impose the divergence constraint on \boldsymbol{b} .

The solenoidal constraint div $\mathbf{b} = 0$ motivates the introduction of an additional Lagrange multiplier r in order to close the variational system and enforce this condition weakly. Since r enters the formulation only through its gradient, it is determined up to an additive constant and we work in a quotient (or zero-mean) space. We therefore take as function spaces for the velocity, pressure, polymeric vector field and scalar multiplier

$$\mathcal{U} := \mathrm{H}^1_0(\Omega)^d, \quad \mathcal{P} := L^2_0(\Omega), \quad \mathcal{B} := \mathrm{H}^1(\Omega)^d, \quad \mathcal{R} := \mathrm{H}^1(\Omega)/\mathbb{R}$$

4.1. Variational formulation. The weak formulation of the system is: for almost every $t \in (0, T)$, seek $(u, p, b, r) \in \mathcal{U} \times \mathcal{P} \times \mathcal{B} \times \mathcal{R}$ such that

(4.3)
$$\operatorname{Re}(\langle \partial_{t}\boldsymbol{u}, \boldsymbol{v} \rangle + \mathcal{O}(\boldsymbol{u}; \boldsymbol{u}, \boldsymbol{v})) + \mathcal{C}(\boldsymbol{v}, p) = -\beta \mathcal{A}(\boldsymbol{u}, \boldsymbol{v}) + \frac{1 - \beta}{\operatorname{Wi}} \left(\frac{1}{2} \mathcal{O}(\boldsymbol{b}; \boldsymbol{b}, \boldsymbol{v}) - \frac{1}{2} \mathcal{O}(\boldsymbol{b}; \boldsymbol{v}, \boldsymbol{b}) \right),$$

$$\langle \partial_{t}\boldsymbol{b}, \boldsymbol{c} \rangle + \mathcal{O}(\boldsymbol{u}; \boldsymbol{b}, \boldsymbol{c}) - \frac{1}{2} \mathcal{O}(\boldsymbol{b}; \boldsymbol{u}, \boldsymbol{c}) + \frac{1}{2} \mathcal{O}(\boldsymbol{b}; \boldsymbol{c}, \boldsymbol{u}) + \mathcal{D}(\boldsymbol{c}, r) = -\frac{1}{\operatorname{Wi}} \langle \boldsymbol{b}, \boldsymbol{c} \rangle,$$

$$\mathcal{C}(\boldsymbol{u}, q) = 0, \qquad \mathcal{D}(\boldsymbol{b}, s) = 0$$

for all test functions $(\boldsymbol{v}, q, \boldsymbol{c}, s) \in \mathcal{U} \times \mathcal{P} \times \mathcal{B} \times \mathcal{R}$.

4.2. **Remark** (Symmetric gradient equivalence). In deriving the weak formulation, and in particular the viscous terms, we use the identity

(4.4)
$$\int_{\Omega} \nabla \boldsymbol{u} : \nabla \boldsymbol{v} d\boldsymbol{x} = \int_{\Omega} \boldsymbol{\varepsilon}(\boldsymbol{u}) : \boldsymbol{\varepsilon}(\boldsymbol{v}) d\boldsymbol{x} + \frac{1}{2} \int_{\Omega} (\operatorname{div} \boldsymbol{u}) (\operatorname{div} \boldsymbol{v}) d\boldsymbol{x},$$

which holds for sufficiently smooth vector fields and appropriate boundary conditions. In particular, for divergence-free test or trial functions the second term vanishes and we obtain

(4.5)
$$\int_{\Omega} \boldsymbol{\varepsilon}(\boldsymbol{u}) : \boldsymbol{\varepsilon}(\boldsymbol{v}) d\boldsymbol{x} = \int_{\Omega_7} \nabla \boldsymbol{u} : \nabla \boldsymbol{v} d\boldsymbol{x} = \mathcal{A}(\boldsymbol{u}, \boldsymbol{v}).$$

This justifies our choice of A in terms of the full gradient rather than the symmetric gradient.

4.3. **Remark** (Skew symmetrisation). At the continuous level, thanks to the fact that u is solenoidal and vanishes on the boundary, the convective form satisfies the antisymmetries

(4.6)
$$\mathcal{O}(\boldsymbol{u};\boldsymbol{u},\boldsymbol{u}) = \mathcal{O}(\boldsymbol{u};\boldsymbol{b},\boldsymbol{b}) = 0.$$

These cancellations will be instrumental in the stability analysis below.

At the discrete level, the choices made for the forms C and D ensure that the discrete velocity is exactly divergence-free, whereas the discrete approximation to \boldsymbol{b} is not. To mitigate the possible negative impact of this asymmetry on stability, we recall that for any solenoidal vector field \boldsymbol{w} , and smooth vector fields \boldsymbol{u} and \boldsymbol{v} (with at least one of them vanishing on the boundary), integration by parts yields

$$\mathcal{O}(\boldsymbol{w}; \boldsymbol{u}, \boldsymbol{v}) = -\mathcal{O}(\boldsymbol{w}; \boldsymbol{v}, \boldsymbol{u}),$$

and hence

(4.7)
$$\mathcal{O}(\boldsymbol{w};\boldsymbol{u},\boldsymbol{v}) = \frac{1}{2} \Big(\mathcal{O}(\boldsymbol{w};\boldsymbol{u},\boldsymbol{v}) - \mathcal{O}(\boldsymbol{w};\boldsymbol{v},\boldsymbol{u}) \Big).$$

This skew-symmetrised representation underlies the convective combinations used in our discretisation and preserves the key cancellation properties at the continuous level.

The weak form (4.3) inherits the dissipative structure of the underlying continuum model, as the following result shows.

4.4. **Theorem** (Energy estimate). Assume that $u_0 \in L^2(\Omega)^d$ and $b_0 \in L^2(\Omega)^d$ are the initial conditions for the velocity and polymeric vector field, respectively. Then any solution of the weak formulation (4.3) satisfies the energy identity

(4.8)
$$\frac{\mathrm{d}}{\mathrm{d}t} \left(\frac{Re}{2} \| \boldsymbol{u} \|_{\mathrm{L}^{2}(\Omega)}^{2} + \frac{1-\beta}{2Wi} \| \boldsymbol{b} \|_{\mathrm{L}^{2}(\Omega)}^{2} \right) = -\beta \| \nabla \boldsymbol{u} \|_{\mathrm{L}^{2}(\Omega)}^{2} - \frac{1-\beta}{Wi^{2}} \| \boldsymbol{b} \|_{\mathrm{L}^{2}(\Omega)}^{2}.$$

Proof To derive (4.8), we take $\mathbf{v} = \mathbf{u}$ in the first equation of (4.3) and $\mathbf{c} = \frac{1-\beta}{\text{Wi}}\mathbf{b}$ in the second one. With q = p and s = r, adding the resulting equations gives

(4.9)
$$\operatorname{Re}(\langle \partial_t \boldsymbol{u}, \boldsymbol{u} \rangle + \mathcal{O}(\boldsymbol{u}; \boldsymbol{u}, \boldsymbol{u})) + \frac{1-\beta}{\operatorname{Wi}} \langle \partial_t \boldsymbol{b}, \boldsymbol{b} \rangle + \frac{1-\beta}{\operatorname{Wi}} \mathcal{O}(\boldsymbol{u}; \boldsymbol{b}, \boldsymbol{b}) - \frac{1-\beta}{\operatorname{Wi}} \left(\frac{1}{2} \mathcal{O}(\boldsymbol{b}; \boldsymbol{u}, \boldsymbol{b}) - \frac{1}{2} \mathcal{O}(\boldsymbol{b}; \boldsymbol{b}, \boldsymbol{u}) \right)$$

$$= -\beta \mathcal{A}(\boldsymbol{u}, \boldsymbol{u}) + \frac{1-\beta}{\operatorname{Wi}} \left(\frac{1}{2} \mathcal{O}(\boldsymbol{b}; \boldsymbol{b}, \boldsymbol{u}) - \frac{1}{2} \mathcal{O}(\boldsymbol{b}; \boldsymbol{u}, \boldsymbol{b}) \right) - \frac{1-\beta}{\operatorname{Wi}^2} \langle \boldsymbol{b}, \boldsymbol{b} \rangle.$$

The convective terms with first argument u vanish by the skew-symmetry (4.6), since u is divergence-free and satisfies the homogeneous boundary conditions. The remaining convective terms, with first argument b, cancel pairwise between the right- and left-hand sides. Using the definitions of A and the inner product then yields (4.8), which completes the proof.

5. Spatial Discretisation

In this section we introduce the spatial discretisation of the problem, using finite element spaces chosen to be compatible with the energy argument above and with the de Rham complex. Let \mathcal{T}_h be a regular subdivision of the domain Ω into disjoint simplicial elements K (triangles in d=2, tetrahedra in d=3). By \mathcal{E}_h we denote the set of all interior (d-1)-dimensional facets (edges in 2D, faces in 3D) associated with the subdivision \mathcal{T}_h . We assume that the subdivision is shape-regular, meaning that the ratio of the diameters of neighbouring elements is uniformly bounded.

For each element $K \in \mathcal{T}_h$ let $\mathcal{P}_p(K)$ denote the polynomials on K of total degree at most p, and define the broken polynomial space

(5.1)
$$\mathcal{P}_p(\mathcal{T}_h) := \left\{ u \in L^2(\Omega) : u|_K \in \mathcal{P}_p(K) \ \forall K \in \mathcal{T}_h \right\}.$$

We write $h_K := \operatorname{diam}(K)$ for the element diameter and collect these into the elementwise constant function $h: \Omega \to \mathbb{R}$, with $h|_K = h_K$. For an interior facet $e = K^+ \cap K^- \subset \mathcal{E}_h$ we set $h|_e = (h_{K^+} + h_{K^-})/2$, while for a boundary facet $e \subset \partial K \cap \partial \Omega$ we set $h|_e = h_K$.

For a vector field ϕ , let K^+ and K^- denote elements sharing an interior facet $e \subset \mathcal{E}_h$, with outward unit normals n^+ and n^- . The tensor jump and average operators are defined, respectively, as

$$\llbracket \boldsymbol{\phi} \rrbracket_{\otimes} := \boldsymbol{\phi}^{+} \otimes \boldsymbol{n}^{+} + \boldsymbol{\phi}^{-} \otimes \boldsymbol{n}^{-}, \qquad \qquad \{ \boldsymbol{\phi} \} := \frac{1}{2} (\boldsymbol{\phi}^{+} + \boldsymbol{\phi}^{-}),$$

where ϕ^{\pm} are the traces of ϕ on e from K^{\pm} . For boundary facets $e \subset \partial \Omega \cap K^+$ we set

Given an advecting field (typically the velocity), we choose the labelling so that K^+ is the upwind element and K^- the downwind one on e. The upwind jump of ϕ across e is then

$$\llbracket \phi \rrbracket := \phi^+ - \phi^-.$$

5.1. Finite element spaces. We use finite element spaces compatible with the de Rham complex to discretise the vector fields, scalar fields and operators. In view of (3.16), for the polymeric vector field \boldsymbol{b} we adopt a curl-conforming discretisation based on the Nédélec finite element spaces of the second kind:

(5.5)
$$\mathcal{B}_h := \mathbb{NED}_p(\Omega, \mathcal{T}_h) = \left\{ \boldsymbol{c} \in H(\operatorname{curl}; \Omega) : \boldsymbol{c}|_K \in \mathcal{P}_p(K)^d, \ \forall K \in \mathcal{T}_h \right\}.$$

Approximating b in \mathcal{B}_h yields a nonconforming approximation with respect to $H^1(\Omega)^d$, since functions in \mathcal{B}_h have continuous tangential components but may be discontinuous in their normal components across element interfaces.

For the velocity field u we employ a divergence-conforming discretisation using the Brezzi-Douglas-Marini finite element spaces:

(5.6)
$$\mathcal{U}_h := \mathbb{BDM}_p(\Omega, \mathcal{T}_h) = \left\{ \boldsymbol{v} \in H(\operatorname{div}; \Omega) : \boldsymbol{v}|_K \in \mathcal{P}_p(K)^d \text{ and } \operatorname{div} \boldsymbol{v} \in \mathcal{P}_{p-1}(K), \ \forall K \in \mathcal{T}_h \right\}.$$

The velocity is approximated in \mathcal{U}_h , so that the normal component of the discrete velocity is continuous across facets, while the tangential component may be discontinuous. Homogeneous velocity boundary conditions are not imposed strongly in \mathcal{U}_h , they will instead be enforced weakly by Nitsche-type terms in the variational formulation below.

For the pressure p and scalar field r, we use standard discontinuous and continuous polynomial spaces, with a zero-mean constraint on the latter:

(5.7)
$$\mathcal{P}_h := \left\{ q_h \in L_0^2(\Omega) : q_h|_K \in \mathcal{P}_{p-1}(K), \ \forall K \in \mathcal{T}_h \right\},$$
$$\mathcal{R}_h := \left\{ s_h \in H^1(\Omega) : s_h|_K \in \mathcal{P}_p(K) \ \forall K \in \mathcal{T}_h, \ \langle s_h, 1 \rangle_{\Omega} = 0 \right\}.$$

On \mathcal{R}_h the seminorm $||s_h||_{\mathcal{R}_h} := ||\nabla s_h||_{L^2(\Omega)}$ is therefore a norm, by Poincaré-Wirtinger.

5.2. **Discrete de Rham complex.** The chosen finite element spaces fit into a discrete de Rham complex, equipped with projection operators that commute with the differential operators:

$$(5.8) \qquad H^{1}(\Omega) \xrightarrow{\nabla} H(\operatorname{curl}; \Omega) \xrightarrow{\operatorname{curl}} H(\operatorname{div}; \Omega) \xrightarrow{\operatorname{div}} L^{2}(\Omega)$$

$$\Pi_{\mathcal{B}_{h}} \downarrow \qquad \Pi_{\mathcal{B}_{h}} \downarrow \qquad \Pi_{\mathcal{U}_{h}} \downarrow \qquad \Pi_{\mathcal{P}_{h}} \downarrow$$

$$\mathcal{R}_{h} \xrightarrow{\nabla} \mathcal{B}_{h} \xrightarrow{\operatorname{curl}} \mathcal{U}_{h} \xrightarrow{\operatorname{div}} \mathcal{P}_{h}$$

Here $\Pi_{\mathcal{R}_h}$, $\Pi_{\mathcal{B}_h}$, $\Pi_{\mathcal{U}_h}$ and $\Pi_{\mathcal{P}_h}$ denote suitable bounded projection operators such that, for instance, $\operatorname{curl}\Pi_{\mathcal{B}_h} = \Pi_{\mathcal{U}_h}\operatorname{curl}$ on $H(\operatorname{curl};\Omega)$ and $\operatorname{div}\Pi_{\mathcal{U}_h} = \Pi_{\mathcal{P}_h}\operatorname{div}$ on $H(\operatorname{div};\Omega)$. This structure ensures that the discrete spaces preserve the compatibility properties of the continuous operators.

5.3. **Remark** (Nonconforming vector spaces). While the discrete spaces for the pressure and Lagrange multiplier, $\mathcal{P}_h \subset \mathcal{P}$ and $\mathcal{R}_h \subset \mathcal{R}$, are conforming to their respective continuous spaces, the vector-valued spaces \mathcal{U}_h and \mathcal{B}_h are not conforming with respect to the H^1 -based spaces used in the weak formulation. Specifically,

$$\mathcal{U}_h \subset H(\operatorname{div};\Omega)$$
 whereas $\mathcal{U} = \operatorname{H}_0^1(\Omega)^d$, $\mathcal{B}_h \subset H(\operatorname{curl};\Omega)$ whereas $\mathcal{B} = \operatorname{H}^1(\Omega)^d$.

This choice is deliberate, the pair $\mathcal{U}_h \times \mathcal{P}_h$ is inf-sup stable (see below), and, moreover, the de Rham structure implies div $\mathcal{U}_h = \mathcal{P}_h$, so that the discrete velocity is exactly divergence-free. The nonconforming but de Rham-compatible choice of \mathcal{U}_h and \mathcal{B}_h is crucial in preserving the structural properties of the continuous problem and plays an important role in the stability analysis of the numerical method.

5.4. **Stabilised discrete forms.** To account for the nonconforming nature of the velocity space, we introduce a stabilised bilinear form for the diffusive term in the weak formulation.

In addition to the interior facets \mathcal{E}_h introduced above, let \mathcal{E}_h^{∂} denote the set of boundary facets $e \subset \partial \Omega$. We write $\mathcal{E}_h^* := \mathcal{E}_h \cup \mathcal{E}_h^{\partial}$ for the collection of all facets, interior and boundary. With the jump and average operators extended to boundary facets as in the previous subsection, we define, for $\boldsymbol{u}_h, \boldsymbol{v}_h \in \mathcal{U}_h$, (5.9)

$$\mathcal{A}_h(\boldsymbol{u}_h, \boldsymbol{v}_h) := \sum_{K \in \mathcal{T}_h} \int_K \nabla \boldsymbol{u}_h : \nabla \boldsymbol{v}_h \, \mathrm{d}\boldsymbol{x} + \sum_{e \in \mathcal{E}_h^*} \int_e \left(\frac{\sigma_e}{h} \, \llbracket \boldsymbol{u}_h \rrbracket_\otimes : \llbracket \boldsymbol{v}_h \rrbracket_\otimes - \llbracket \nabla \boldsymbol{u}_h \rrbracket : \llbracket \boldsymbol{v}_h \rrbracket_\otimes - \llbracket \nabla \boldsymbol{v}_h \rrbracket : \llbracket \boldsymbol{u}_h \rrbracket_\otimes \right) \, \mathrm{d}\boldsymbol{s},$$

where $\sigma_e > 0$ is a facet-wise stabilisation parameter penalising tangential discontinuities. On boundary facets the definition of the jump and average reduces to $[\![u_h]\!]_{\otimes} = u_h \otimes n$ and $\{\![\nabla u_h]\!]_{\otimes} = \nabla u_h$, so that the same form provides a Nitsche-type weak enforcement of the homogeneous velocity boundary condition. In practice we take

$$\sigma_e = \begin{cases} \sigma_{\rm i}, & e \text{ interior,} \\ \sigma_{\rm b}, & e \subset \partial \Omega, \end{cases}$$

with constants $\sigma_i, \sigma_b > 0$.

5.5. Lemma (DG norm and coercivity). The DG norm $\|\cdot\|_{1,h}$ for a discrete velocity field $v_h \in \mathcal{U}_h$ is defined as

(5.10)
$$\|\boldsymbol{v}_h\|_{1,h}^2 := \sum_{K \in \mathcal{T}_h} \|\nabla \boldsymbol{v}_h\|_{L^2(K)}^2 + \sum_{e \in \mathcal{E}_*^*} \frac{1}{h} \|[\boldsymbol{v}_h]_{\otimes}\|_{L^2(e)}^2.$$

The bilinear form A_h is coercive with respect to this norm: for σ chosen large enough, and for any $u_h \in \mathcal{U}_h$, it holds that (see, for example, [3])

(5.11)
$$\mathcal{A}_h(\boldsymbol{u}_h, \boldsymbol{u}_h) \ge \alpha \|\boldsymbol{u}_h\|_{1,h}^2,$$

where $\alpha > 0$ is a constant independent of h.

Below we state the inf-sup conditions associated with the pairs $\mathcal{U}_h \times \mathcal{P}_h$ and $\mathcal{B}_h \times \mathcal{R}_h$. Although their proofs are standard, and follow from the results in [9, Section 2.5] (see also [26, Lemma 7 and Proposition 10]), we summarise them here for completeness.

- 5.6. **Lemma** (Inf-sup conditions). Let $(\mathcal{U}_h, \mathcal{P}_h)$ and $(\mathcal{B}_h, \mathcal{R}_h)$ denote the finite element spaces for the velocity-pressure and polymeric vector field-Lagrange multiplier pairs, respectively. Then:
 - (1) There exists a constant $C_1 > 0$, independent of h, such that

(5.12)
$$\sup_{\boldsymbol{v}_h \in \mathcal{U}_h} \frac{\mathcal{C}(\boldsymbol{v}_h, q_h)}{\|\boldsymbol{v}_h\|_{1,h}} \ge C_1 \|q_h\|_{L^2(\Omega)} \quad \forall \, q_h \in \mathcal{P}_h.$$

(2) For all $s_h \in \mathcal{R}_h$ it holds that

(5.13)
$$\sup_{\boldsymbol{c}_h \in \mathcal{B}_h} \frac{\mathcal{D}(\boldsymbol{c}_h, s_h)}{\|\boldsymbol{c}_h\|_{L^2(\Omega)}} \ge \|\nabla s_h\|_{L^2(\Omega)}.$$

In particular, since \mathcal{R}_h consists of zero-mean functions, the quantity $\|\nabla s_h\|_{L^2(\Omega)}$ defines a norm on \mathcal{R}_h by the Poincaré-Wirtinger inequality.

Proof For the first inf-sup condition, let $q_h \in \mathcal{P}_h$. By the standard surjectivity of the divergence operator on $L_0^2(\Omega)$, there exists $\boldsymbol{v} \in \mathrm{H}_0^1(\Omega)^d$ such that $\operatorname{div} \boldsymbol{v} = q_h$ in Ω and $\|\boldsymbol{v}\|_{H^1(\Omega)} \leq C\|q_h\|_{L^2(\Omega)}$ for some constant C > 0 independent of h. Let $\Pi_{\mathcal{U}_h} : \mathrm{H}_0^1(\Omega)^d \to \mathcal{U}_h$ denote a Fortin operator satisfying the commuting diagram property

(5.14)
$$\operatorname{div}(\Pi_{\mathcal{U}_h} \boldsymbol{v}) = \Pi_{\mathcal{P}_h}(\operatorname{div} \boldsymbol{v}),$$

where $\Pi_{\mathcal{P}_h}$ is the L^2 -projection onto \mathcal{P}_h . Since $q_h \in \mathcal{P}_h$ and \mathcal{P}_h consists of functions with zero mean, $\Pi_{\mathcal{P}_h} q_h = q_h$, and thus

(5.15)
$$\mathcal{C}(\Pi_{\mathcal{U}_h} \boldsymbol{v}, q_h) = \mathcal{C}(\boldsymbol{v}, q_h) = \|q_h\|_{L^2(\Omega)}^2.$$

Moreover, by the $H^1(K)$ -stability of $\Pi_{\mathcal{U}_h}$ (see [9, Proposition 2.5.1]) we obtain

(5.16)
$$\|\Pi_{\mathcal{U}_{h}} v\|_{1,h} \leq C \|v\|_{H^{1}(\Omega)} \leq C \|q_{h}\|_{L^{2}(\Omega)},$$

with a constant C independent of h. Taking $\boldsymbol{v}_h = \Pi_{\mathcal{U}_h} \boldsymbol{v}$ in (5.12) yields the desired bound for C.

For the second inf-sup condition, let $s_h \in \mathcal{R}_h$ be given and define

$$(5.17) c_h := \nabla s_h.$$

By the discrete de Rham complex we have $c_h \in \mathcal{B}_h$, and moreover

(5.18)
$$\|\boldsymbol{c}_h\|_{\mathrm{L}^2(\Omega)} = \|\nabla s_h\|_{\mathrm{L}^2(\Omega)}, \qquad \mathcal{D}(\boldsymbol{c}_h, s_h) = \|\nabla s_h\|_{\mathrm{L}^2(\Omega)}^2.$$

Hence

(5.19)
$$\frac{\mathcal{D}(\boldsymbol{c}_h, s_h)}{\|\boldsymbol{c}_h\|_{L^2(\Omega)}} = \|\nabla s_h\|_{L^2(\Omega)}.$$

Taking the supremum over all $c_h \in \mathcal{B}_h$ gives the asserted bound for \mathcal{D} , and the proof is complete.

For \boldsymbol{w}_h , \boldsymbol{u}_h and \boldsymbol{v}_h , the upwind discretisation of the convective term is defined as (5.20)

$$\mathcal{O}_h(\boldsymbol{w}_h;\boldsymbol{u}_h,\boldsymbol{v}_h) := \sum_{K \in \mathcal{T}_h} \int_K (\boldsymbol{w}_h \cdot \nabla) \, \boldsymbol{u}_h \cdot \boldsymbol{v}_h \mathrm{d}\boldsymbol{x} - \int_{\mathcal{E}_h} \left((\boldsymbol{w}_h \cdot \boldsymbol{n}) \, \{\!\!\{ \boldsymbol{u}_h \}\!\!\} \cdot [\!\!\{ \boldsymbol{v}_h \rfloor\!\!] - \frac{\mu}{2} |\boldsymbol{w}_h \cdot \boldsymbol{n}| \, [\!\!\{ \boldsymbol{u}_h \rfloor\!\!] \cdot [\!\!\{ \boldsymbol{v}_h \rfloor\!\!] \right) \mathrm{d}\boldsymbol{s},$$

where n is the unit normal on each interior facet and $\mu > 0$ is an upwind parameter (in the computations below we take $\mu = 1$).

We now summarise stability and continuity properties of the upwind convective form. For proofs we refer to, for example, [17, Propositions 4.2 and 4.3].

5.7. **Theorem** (Properties of \mathcal{O}_h). Let $\boldsymbol{w} \in H^1(\mathcal{T}_h)^d \cap H(\operatorname{div}; \Omega)$ with $\operatorname{div} \boldsymbol{w} = 0$ in Ω and $\boldsymbol{w} \cdot \boldsymbol{n} = 0$ on $\partial \Omega$, and let $\boldsymbol{v}_h \in \mathcal{P}_p(\mathcal{T}_h)^d$. Then the convective term satisfies

(5.21)
$$\mathcal{O}_h(\boldsymbol{w}; \boldsymbol{v}_h, \boldsymbol{v}_h) = \frac{\mu}{2} \sum_{e \in \mathcal{E}_h} \int_e |\boldsymbol{w} \cdot \boldsymbol{n}| \, \|\boldsymbol{v}_h\|^2 \, \mathrm{d}s.$$

Furthermore, for any $\mathbf{u} \in H_0^1(\Omega)^d + \mathcal{P}_p(\mathcal{T}_h)^d$ and any \mathbf{w}, \mathbf{w}_1 as above, there exists a constant C > 0, independent of h, such that

$$\left| \mathcal{O}_h(\boldsymbol{w}; \boldsymbol{u}, \boldsymbol{v}_h) - \mathcal{O}_h(\boldsymbol{w}_1; \boldsymbol{u}, \boldsymbol{v}_h) \right| \le C \|\boldsymbol{w} - \boldsymbol{w}_1\|_{1,h} \|\boldsymbol{u}\|_{1,h} \|\boldsymbol{v}_h\|_{1,h}.$$

5.8. Steady-state weak formulation. In this section we analyse existence and stability for the steady-state version of the discrete problem. For this section only, we allow a non-zero body force f in the momentum equation and define the linear functional

$$F(\boldsymbol{v}_h, \boldsymbol{c}_h) = \langle \boldsymbol{f}, \boldsymbol{v}_h \rangle.$$

We introduce the nonlinear form

(5.23)
$$\mathfrak{A}((\boldsymbol{u}_h, \boldsymbol{b}_h); (\boldsymbol{v}_h, \boldsymbol{c}_h)) := \operatorname{Re}\mathcal{O}_h(\boldsymbol{u}_h; \boldsymbol{u}_h, \boldsymbol{v}_h) + \beta \mathcal{A}_h(\boldsymbol{u}_h, \boldsymbol{v}_h) - \frac{1-\beta}{2\operatorname{Wi}} \left(\mathcal{O}_h(\boldsymbol{b}_h; \boldsymbol{b}_h, \boldsymbol{v}_h) - \mathcal{O}_h(\boldsymbol{b}_h; \boldsymbol{v}_h, \boldsymbol{b}_h) \right) \\ + \frac{1-\beta}{2\operatorname{Wi}} \left(\mathcal{O}_h(\boldsymbol{u}_h; \boldsymbol{b}_h, \boldsymbol{c}_h) - \frac{1}{2}\mathcal{O}_h(\boldsymbol{b}_h; \boldsymbol{u}_h, \boldsymbol{c}_h) + \frac{1}{2}\mathcal{O}_h(\boldsymbol{b}_h; \boldsymbol{c}_h, \boldsymbol{u}_h) \right) + \frac{1-\beta}{\operatorname{Wi}^2} \left\langle \boldsymbol{b}_h, \boldsymbol{c}_h \right\rangle,$$

and the bilinear form

$$\mathfrak{B}((\boldsymbol{v}_h, \boldsymbol{c}_h), (q_h, s_h)) := \mathcal{C}(\boldsymbol{v}_h, q_h) + \mathcal{D}(\boldsymbol{c}_h, s_h).$$

The steady-state discrete problem then reads: find $(u_h, p_h, b_h, r_h) \in \mathcal{U}_h \times \mathcal{P}_h \times \mathcal{B}_h \times \mathcal{R}_h$ such that

(5.25)
$$\mathfrak{A}((\boldsymbol{u}_h, \boldsymbol{b}_h); (\boldsymbol{v}_h, \boldsymbol{c}_h)) + \mathfrak{B}((\boldsymbol{v}_h, \boldsymbol{c}_h), (p_h, r_h)) = F(\boldsymbol{v}_h, \boldsymbol{c}_h), \\ \mathfrak{B}((\boldsymbol{\psi}_h, \boldsymbol{b}_h), (q_h, s_h)) = 0,$$

for all $(\boldsymbol{v}_h, q_h, \boldsymbol{c}_h, s_h) \in \mathcal{U}_h \times \mathcal{P}_h \times \mathcal{B}_h \times \mathcal{R}_h$.

We equip the discrete spaces with the norms

5.9. Lemma (Discrete stationary inf-sup). There exists a constant C > 0, independent of h, such that

(5.27)
$$\sup_{(\boldsymbol{v}_h, \boldsymbol{c}_h) \in \mathcal{U}_h \times \mathcal{B}_h} \frac{\mathfrak{B}((\boldsymbol{v}_h, \boldsymbol{c}_h), (q_h, s_h))}{\|(\boldsymbol{v}_h, \boldsymbol{c}_h)\|_{X_h}} \ge C \|(q_h, s_h)\|_{Y_h}, \qquad \forall (q_h, s_h) \in \mathcal{P}_h \times \mathcal{R}_h.$$

Furthermore, there exists a constant C > 0, independent of h, such that

$$\mathfrak{A}((\boldsymbol{v}_h, \boldsymbol{c}_h); (\boldsymbol{v}_h, \boldsymbol{c}_h)) \ge C \|(\boldsymbol{v}_h, \boldsymbol{c}_h)\|_{X_h}^2, \qquad \forall (\boldsymbol{v}_h, \boldsymbol{c}_h) \in \mathcal{U}_h \times \mathcal{B}_h.$$

Proof. The inf-sup estimate (5.27) is a direct consequence of Lemma 5.6 and the definitions of the norms $\|\cdot\|_{X_h}$ and $\|\cdot\|_{Y_h}$.

To prove (5.28), let $(\boldsymbol{v}_h, \boldsymbol{c}_h) \in \mathcal{U}_h \times \mathcal{B}_h$. Using the coercivity of \mathcal{A}_h and the positivity properties of \mathcal{O}_h from Theorem 5.7, together with the definition of \mathfrak{A} , we obtain

$$\mathfrak{A}((\boldsymbol{v}_{h},\boldsymbol{c}_{h});(\boldsymbol{v}_{h},\boldsymbol{c}_{h})) \geq \alpha\beta \|\boldsymbol{v}_{h}\|_{1,h}^{2} + \frac{1-\beta}{\mathrm{Wi}^{2}} \|\boldsymbol{c}_{h}\|_{\mathrm{L}^{2}(\Omega)}^{2}$$

$$+ \frac{1}{2} \sum_{e \in \mathcal{E}_{h}} \int_{e} |\boldsymbol{v}_{h} \cdot \boldsymbol{n}| \left(\mu \mathrm{Re} \|\boldsymbol{v}_{h}\|^{2} + (1-\beta) \mathrm{Wi}^{-1} \|\boldsymbol{c}_{h}\|^{2}\right) ds$$

$$\geq \alpha\beta \|\boldsymbol{v}_{h}\|_{1,h}^{2} + \frac{1-\beta}{\mathrm{Wi}^{2}} \|\boldsymbol{c}_{h}\|_{\mathrm{L}^{2}(\Omega)}^{2}.$$

This shows that \mathfrak{A} is coercive on $\mathcal{U}_h \times \mathcal{B}_h$ with respect to $\|\cdot\|_{X_h}$, and proves (5.28).

From Lemma 5.9, a standard application of Brouwer's fixed-point theorem (see, for example, [7, Theorem 3.1.13]) yields the steady-state existence result stated below.

5.10. Corollary (Existence of the discrete problem). Under the assumptions of Lemma 5.9, there exists at least one solution $(\mathbf{u}_h, p_h, \mathbf{b}_h, r_h) \in \mathcal{U}_h \times \mathcal{P}_h \times \mathcal{B}_h \times \mathcal{R}_h$ to the discrete system (5.25). In addition, there exists a constant C > 0, depending only on the physical parameters of the problem and on the domain Ω , such that

$$\|(\boldsymbol{u}_h, p_h, \boldsymbol{b}_h, r_h)\|_{X_h \times Y_h} \le C \|F\|_{X_h^*}.$$

- 5.11. **Remark** (Uniqueness). Uniqueness of the discrete solution can only be inferred if Re, Wi and the data are sufficiently small. Such smallness conditions are well known already in the incompressible Navier-Stokes regime, where uniqueness holds at low Re but may fail at high Re due to the growth of nonlinear effects [7]. In the present coupled system, a comparable balance between dissipation and nonlinear growth is required to guarantee uniqueness.
- 5.12. Spatially semidiscrete weak formulation. Given solenoidal initial conditions $(\boldsymbol{u}_0, \boldsymbol{b}_0) \in \mathcal{U} \times \mathcal{B}$ with div $\boldsymbol{u}_0 = 0$ and div $\boldsymbol{b}_0 = 0$ in Ω , we define discrete initial data by

$$oldsymbol{u}_{h,0} := \Pi_{\mathcal{U}_h} oldsymbol{u}_0, \qquad oldsymbol{b}_{h,0} := \Pi_{\mathcal{B}_h} oldsymbol{b}_0,$$

where $\Pi_{\mathcal{U}_h}$ and $\Pi_{\mathcal{B}_h}$ are the commuting projections associated with the discrete de Rham complex. The spatially semidiscrete problem then reads: find $(\boldsymbol{u}_h, p_h, \boldsymbol{b}_h, r_h)(t) \in \mathcal{U}_h \times \mathcal{P}_h \times \mathcal{B}_h \times \mathcal{R}_h$ such that

(5.31)
$$\operatorname{Re} \langle \partial_t \boldsymbol{u}_h, \boldsymbol{v}_h \rangle + \langle \partial_t \boldsymbol{b}_h, \boldsymbol{c}_h \rangle + \mathfrak{A}((\boldsymbol{u}_h, \boldsymbol{b}_h), (\boldsymbol{v}_h, \boldsymbol{c}_h)) + \mathfrak{B}((\boldsymbol{v}_h, \boldsymbol{c}_h), (p_h, r_h)) = 0, \\ \mathfrak{B}((\boldsymbol{u}_h, \boldsymbol{b}_h), (q_h, s_h)) = 0,$$

for all test functions $(\boldsymbol{v}_h, q_h, \boldsymbol{c}_h, s_h) \in \mathcal{U}_h \times \mathcal{P}_h \times \mathcal{B}_h \times \mathcal{R}_h$, with initial data $\boldsymbol{u}_h(0) = \boldsymbol{u}_{h,0}$ and $\boldsymbol{b}_h(0) = \boldsymbol{b}_{h,0}$.

5.13. **Theorem** (Existence, uniqueness and energy law for the spatially semidiscrete problem). Assume that $(\mathbf{u}_0, \mathbf{b}_0) \in \mathcal{U} \times \mathcal{B}$ with div $\mathbf{u}_0 = 0$ and div $\mathbf{b}_0 = 0$ in Ω , and let the discrete initial data be given by the projections $\mathbf{u}_{h,0}$ and $\mathbf{b}_{h,0}$ defined above. Then there exists a unique solution

$$(\boldsymbol{u}_h(t), p_h(t), \boldsymbol{b}_h(t), r_h(t)) \in \mathcal{U}_h \times \mathcal{P}_h \times \mathcal{B}_h \times \mathcal{R}_h$$

to the spatially semidiscrete problem (5.31) on [0,T], depending continuously on the initial data.

Moreover, the solution satisfies the discrete energy law

$$\begin{split} \frac{\mathrm{d}}{\mathrm{d}t} \left(\frac{\mathrm{R}e}{2} \| \boldsymbol{u}_h \|_{L^2(\Omega)}^2 + \frac{1-\beta}{2Wi} \| \boldsymbol{b}_h \|_{L^2(\Omega)}^2 \right) &= -\beta \mathcal{A}_h(\boldsymbol{u}_h, \boldsymbol{u}_h) - \frac{1-\beta}{Wi^2} \| \boldsymbol{b}_h \|_{L^2(\Omega)}^2 \\ &- \mathrm{R}e \mathcal{O}_h(\boldsymbol{u}_h; \boldsymbol{u}_h, \boldsymbol{u}_h) - \frac{1-\beta}{Wi} \mathcal{O}_h(\boldsymbol{u}_h; \boldsymbol{b}_h, \boldsymbol{b}_h) \,, \end{split}$$

so that, in particular, the discrete total energy is non-increasing in time.

5.14. **Remark** (Discrete dissipation). Comparing the discrete energy law above with the continuous energy law (4.8), we observe the additional dissipative contributions introduced by the upwind discretisation of the convective terms. In particular, the facet terms in $\mathcal{O}_h(\boldsymbol{u}_h;\cdot,\cdot)$ provide extra damping through jump penalisation, which is absent at the continuous level.

Proof of Theorem 5.13 To derive the discrete energy law, in (5.31) we take $\mathbf{v}_h = \mathbf{u}_h$ in the first equation and $\mathbf{c}_h = \frac{1-\beta}{\mathrm{Wi}} \mathbf{b}_h$ in the second one, and add the resulting identities. Choosing $q_h = p_h$ and $s_h = r_h$, and using the cancellation of the skew-symmetric convective terms together with the coercivity of \mathcal{A}_h and the properties of \mathcal{O}_h from Theorem 5.7, yields the stated discrete energy law.

For well-posedness, we follow the approach in, for example, [13, Section 5]. We first introduce the discrete kernel

$$(5.32) \mathcal{Z}_h := \{ (\boldsymbol{v}_h, \boldsymbol{c}_h) \in \mathcal{U}_h \times \mathcal{B}_h : \mathfrak{B}((\boldsymbol{v}_h, \boldsymbol{c}_h), (q_h, s_h)) = 0 \ \forall (q_h, s_h) \in \mathcal{P}_h \times \mathcal{R}_h \}.$$

The semidiscrete weak formulation (5.31) is equivalent to an abstract system of ODEs posed on \mathcal{Z}_h : find $z_h(t) \in \mathcal{Z}_h$ such that $z_h(0) = (u_{h,0}, b_{h,0})$ and

$$\mathbf{M}\frac{\mathrm{d}\mathbf{z}_h}{\mathrm{d}t} + \mathbf{A}(\mathbf{z}_h) = 0,$$

where M is the (symmetric) positive definite mass matrix associated with the L^2 inner product, and $A(z_h)$ is the nonlinear operator induced by \mathfrak{A} restricted to \mathcal{Z}_h .

Using Theorem 5.7 and the boundedness of the remaining terms in \mathfrak{A} , we infer that A is Lipschitz continuous on \mathcal{Z}_h with respect to the $\|\cdot\|_{X_h}$ -norm, that is,

(5.34)
$$\|\boldsymbol{A}(\boldsymbol{z}_h) - \boldsymbol{A}(\boldsymbol{z}_h')\|_{X_h^*} \leq L \|\boldsymbol{z}_h - \boldsymbol{z}_h'\|_{X_h} ,$$

for some constant L > 0 independent of h. The Picard-Lindelöf theorem then guarantees the existence and uniqueness of a solution $z_h(t)$ on [0,T], and therefore of $(u_h(t), p_h(t), b_h(t), r_h(t))$, completing the proof.

6. An IMEX temporal discretisation

The choice of temporal discretisation impacts the properties of the fully discrete energy law. Structure-preserving schemes, such as the Crank-Nicolson method, can be used to retain a discrete analogue of the continuum energy balance. On the other hand, dissipative schemes such as backward differentiation formulae introduce additional numerical diffusion. This added dissipation can be beneficial in flows where excessive energy growth from nonlinearities, such as elastic turbulence, must be controlled. However, these methods are inherently nonlinear, requiring iterative solvers at each time step and thus increasing computational cost.

In this section we introduce an implicit-explicit (IMEX) method that preserves a discrete energy law while keeping the scheme linear at each time step, offering a balance between stability and computational efficiency.

To discretise the system in time, let $N \in \mathbb{N}$ be the number of time steps, and define temporal nodes $0 = t^0 < t^1 < \cdots < t^N = T$. For simplicity we take a uniform time step $\tau := t^n - t^{n-1}$, and for a generic function u write $u^n := u(t^n)$ for its value at time t^n .

6.1. **Time-stepping scheme.** Given discrete initial conditions $\boldsymbol{u}_h^0 \in \mathcal{U}_h$ and $\boldsymbol{b}_h^0 \in \mathcal{B}_h$, for each time step $n = 0, 1, 2, \dots, N-1$ we seek $(\boldsymbol{u}_h^{n+1}, p_h^{n+1}, \boldsymbol{b}_h^{n+1}, r_h^{n+1}) \in \mathcal{U}_h \times \mathcal{P}_h \times \mathcal{B}_h \times \mathcal{R}_h$ such that

$$\operatorname{Re}\left\langle \frac{\boldsymbol{u}_{h}^{n+1} - \boldsymbol{u}_{h}^{n}}{\tau}, \boldsymbol{v}_{h} \right\rangle + \operatorname{Re}\mathcal{O}_{h}(\boldsymbol{u}_{h}^{n}; \boldsymbol{u}_{h}^{n+1}, \boldsymbol{v}_{h}) + \mathcal{C}(\boldsymbol{v}_{h}, p_{h}^{n+1})$$

$$= -\beta \mathcal{A}_{h}(\boldsymbol{u}_{h}^{n+1}, \boldsymbol{v}_{h}) + \frac{1 - \beta}{2\operatorname{Wi}} \mathcal{O}_{h}(\boldsymbol{b}_{h}^{n}; \boldsymbol{b}_{h}^{n+1}, \boldsymbol{v}_{h}) - \frac{1 - \beta}{2\operatorname{Wi}} \mathcal{O}_{h}(\boldsymbol{b}_{h}^{n}; \boldsymbol{v}_{h}, \boldsymbol{b}_{h}^{n+1}),$$

$$\left\langle \frac{\boldsymbol{b}_{h}^{n+1} - \boldsymbol{b}_{h}^{n}}{\tau}, \boldsymbol{c}_{h} \right\rangle + \mathcal{O}_{h}(\boldsymbol{u}_{h}^{n}; \boldsymbol{b}_{h}^{n+1}, \boldsymbol{c}_{h}) - \frac{1}{2}\mathcal{O}_{h}(\boldsymbol{b}_{h}^{n}; \boldsymbol{u}_{h}^{n+1}, \boldsymbol{c}_{h}) + \frac{1}{2}\mathcal{O}_{h}(\boldsymbol{b}_{h}^{n}; \boldsymbol{c}_{h}, \boldsymbol{u}_{h}^{n+1})$$

$$+ \mathcal{D}(\boldsymbol{c}_{h}, r_{h}^{n+1}) + \frac{1}{\operatorname{Wi}} \left\langle \boldsymbol{b}_{h}^{n+1}, \boldsymbol{c}_{h} \right\rangle = 0,$$

$$\mathcal{C}(\boldsymbol{u}_{h}^{n+1}, \boldsymbol{q}_{h}) = 0,$$

$$\mathcal{D}(\boldsymbol{b}_{h}^{n+1}, \boldsymbol{s}_{h}) = 0,$$

for all test functions $(\boldsymbol{v}_h, q_h, \boldsymbol{c}_h, s_h) \in \mathcal{U}_h \times \mathcal{P}_h \times \mathcal{B}_h \times \mathcal{R}_h$.

- 6.2. **Remark** (Consistency). The IMEX scheme (6.1) is first-order accurate in time due to the explicit treatment of the nonlinear terms. Higher-order temporal accuracy may be achieved by replacing the Euler time-stepping with a higher-order IMEX Runge-Kutta method, as described in [4].
- 6.3. **Theorem** (Existence, uniqueness and discrete energy law). Let $(\boldsymbol{u}^0, \boldsymbol{b}^0) \in \mathcal{U} \times \mathcal{B}$ be initial conditions satisfying the divergence-free constraints, and let the corresponding discrete initial data be $\boldsymbol{u}_h^0 = \Pi_{\mathcal{U}_h} \boldsymbol{u}^0$ and $\boldsymbol{b}_h^0 = \Pi_{\mathcal{B}_h} \boldsymbol{b}^0$. Then, for each $n = 0, 1, \ldots, N-1$ there exists a unique solution $(\boldsymbol{u}_h^{n+1}, p_h^{n+1}, \boldsymbol{b}_h^{n+1}, r_h^{n+1}) \in \mathcal{U}_h \times \mathcal{P}_h \times \mathcal{B}_h \times \mathcal{R}_h$ to the fully discrete system (6.1).

Furthermore, the solution satisfies the discrete energy law

$$(6.2) \quad \frac{Re}{2} \|\boldsymbol{u}_{h}^{n+1}\|_{L^{2}(\Omega)}^{2} + \frac{1-\beta}{2Wi} \|\boldsymbol{b}_{h}^{n+1}\|_{L^{2}(\Omega)}^{2} = \frac{Re}{2} \|\boldsymbol{u}_{h}^{0}\|_{L^{2}(\Omega)}^{2} + \frac{1-\beta}{2Wi} \|\boldsymbol{b}_{h}^{0}\|_{L^{2}(\Omega)}^{2} - \sum_{j=0}^{n} \left(\frac{Re}{2} \|\boldsymbol{u}_{h}^{j+1} - \boldsymbol{u}_{h}^{j}\|_{L^{2}(\Omega)}^{2} + \frac{1-\beta}{2Wi} \|\boldsymbol{b}_{h}^{j+1} - \boldsymbol{b}_{h}^{j}\|_{L^{2}(\Omega)}^{2}\right) - \tau \sum_{j=0}^{n} \left(\beta \mathcal{A}_{h}(\boldsymbol{u}_{h}^{j+1}, \boldsymbol{u}_{h}^{j+1}) + \frac{1-\beta}{Wi^{2}} \|\boldsymbol{b}_{h}^{j+1}\|_{L^{2}(\Omega)}^{2} \right) + \sum_{e \in \mathcal{E}_{h}} \int_{e} \left(\mu Re |\boldsymbol{u}_{h}^{j} \cdot \boldsymbol{n}| \|\boldsymbol{u}_{h}^{j+1}\|^{2} + \frac{1-\beta}{Wi} |\boldsymbol{u}_{h}^{j} \cdot \boldsymbol{n}| \|\boldsymbol{b}_{h}^{j+1}\|^{2}\right) ds \right).$$

Proof We first derive the discrete energy law. In (6.1), take $\boldsymbol{v}_h = \boldsymbol{u}_h^{n+1}$ in the first equation and $\boldsymbol{c}_h = \frac{1-\beta}{\mathrm{Wi}}\boldsymbol{b}_h^{n+1}$ in the second equation, and add the resulting identities. Using \mathcal{C} and \mathcal{D} with $(q_h, s_h) = (p_h^{n+1}, r_h^{n+1})$ gives

$$(6.3) \operatorname{Re}\left\langle \frac{\boldsymbol{u}_{h}^{n+1} - \boldsymbol{u}_{h}^{n}}{\tau}, \boldsymbol{u}_{h}^{n+1} \right\rangle + \frac{1 - \beta}{\operatorname{Wi}} \left\langle \frac{\boldsymbol{b}_{h}^{n+1} - \boldsymbol{b}_{h}^{n}}{\tau}, \boldsymbol{b}_{h}^{n+1} \right\rangle + \beta \mathcal{A}_{h}(\boldsymbol{u}_{h}^{n+1}, \boldsymbol{u}_{h}^{n+1}) \\ + \frac{1 - \beta}{\operatorname{Wi}^{2}} \left\| \boldsymbol{b}_{h}^{n+1} \right\|_{\operatorname{L}^{2}(\Omega)}^{2} + \sum_{e \in \mathcal{E}_{h}} \int_{e} \left(\mu \operatorname{Re} |\boldsymbol{u}_{h}^{n} \cdot \boldsymbol{n}| \left\| \boldsymbol{u}_{h}^{n+1} \right\|^{2} + \frac{1 - \beta}{\operatorname{Wi}} |\boldsymbol{u}_{h}^{n} \cdot \boldsymbol{n}| \left\| \boldsymbol{b}_{h}^{n+1} \right\|^{2} \right) \mathrm{d}s = 0.$$

The time-derivative terms are rewritten using

$$(x-y)x = \frac{1}{2}x^2 - \frac{1}{2}y^2 + \frac{1}{2}(x-y)^2,$$

which yields

$$(6.4) \quad \frac{\text{Re}}{2\tau} \left(\left\| \boldsymbol{u}_{h}^{n+1} \right\|_{\text{L}^{2}(\Omega)}^{2} - \left\| \boldsymbol{u}_{h}^{n} \right\|_{\text{L}^{2}(\Omega)}^{2} \right) + \frac{1 - \beta}{2\tau \text{Wi}} \left(\left\| \boldsymbol{b}_{h}^{n+1} \right\|_{\text{L}^{2}(\Omega)}^{2} - \left\| \boldsymbol{b}_{h}^{n} \right\|_{\text{L}^{2}(\Omega)}^{2} \right) \\ + \frac{\text{Re}}{2} \left\| \boldsymbol{u}_{h}^{n+1} - \boldsymbol{u}_{h}^{n} \right\|_{\text{L}^{2}(\Omega)}^{2} + \frac{1 - \beta}{2\text{Wi}} \left\| \boldsymbol{b}_{h}^{n+1} - \boldsymbol{b}_{h}^{n} \right\|_{\text{L}^{2}(\Omega)}^{2} \\ + \beta \mathcal{A}_{h} (\boldsymbol{u}_{h}^{n+1}, \boldsymbol{u}_{h}^{n+1}) + \frac{1 - \beta}{\text{Wi}^{2}} \left\| \boldsymbol{b}_{h}^{n+1} \right\|_{\text{L}^{2}(\Omega)}^{2} + \sum_{e \in \mathcal{E}_{1}} \int_{e} \left(\mu \text{Re} |\boldsymbol{u}_{h}^{n} \cdot \boldsymbol{n}| \left\| \boldsymbol{u}_{h}^{n+1} \right\|^{2} + \frac{1 - \beta}{\text{Wi}} |\boldsymbol{u}_{h}^{n} \cdot \boldsymbol{n}| \left\| \boldsymbol{b}_{h}^{n+1} \right\|^{2} \right) ds = 0.$$

Multiplying by τ and rearranging gives a one-step energy balance. Summing this identity from j = 0 to j = n and telescoping the leading terms yields (6.2).

To establish existence and uniqueness at each time step, we observe that (6.1) defines, for fixed data $(\boldsymbol{u}_h^n, \boldsymbol{b}_h^n)$, a linear system for $(\boldsymbol{u}_h^{n+1}, p_h^{n+1}, \boldsymbol{b}_h^{n+1}, r_h^{n+1})$. The discrete energy identity implies that if the right-hand side corresponding to the previous time step is homogeneous, then the only solution is the trivial one, so the associated linear operator is injective. Since the operator acts on a finite-dimensional space, injectivity implies bijectivity, and thus a unique solution exists for each time step. By induction on n, this gives existence and uniqueness of the fully discrete solution sequence.

7. Numerical Experiments

In this section we numerically investigate the IMEX discretisation (6.1), implemented in the FEniCS finite element software. In Section 7.1 we verify convergence, and in Sections 7.2-7.4 we demonstrate the stability of the method in challenging physically-inspired experiments for a range of Weissenberg numbers. We focus on low Reynolds number regimes and examine the impact of varying the elasticity ratio β and the Weissenberg number Wi.

For each of the physically-inspired experiments we first consider the discretisation (6.1) applied to the reduced system (3.15) as derived in Section 3. We then repeat the experiment with an additional explicit term

$$\frac{1-\gamma}{\text{Wi}} \, \frac{\boldsymbol{b}_h^n}{|\boldsymbol{b}_h^n|}$$

on the right-hand side of the equation for \boldsymbol{b}_h^{n+1} (with the convention that this contribution is set to zero when $\boldsymbol{b}_h^n=\mathbf{0}$), where $\gamma=10^{-6}$. In the full Oldroyd–B model the relaxation term $-\mathrm{Wi}^{-1}(\boldsymbol{\sigma}-\boldsymbol{I})$ drives the conformation towards the isotropic state $\boldsymbol{\sigma}=\boldsymbol{I}$, so that at rest the principal eigenvalue tends to 1. In the strong-stretch, uniaxial reduction used here, where $\boldsymbol{\sigma}\approx\boldsymbol{b}\otimes\boldsymbol{b}$ and the identity contribution has been neglected, the reduced equation contains only the damping $-\mathrm{Wi}^{-1}\boldsymbol{b}$ and therefore has an equilibrium at $\boldsymbol{b}=\mathbf{0}$, corresponding to vanishing polymeric stress and an effectively Newtonian response. The additional explicit term can be viewed as a simple surrogate for the omitted identity contribution: in the absence of flow it tends to stabilise the amplitude $|\boldsymbol{b}|$ near a non-zero value of order one (roughly $|\boldsymbol{b}|\approx 1-\gamma$), while leaving the directional dynamics governed by transport and stretching. Our numerical results show that including this term yields flow patterns that are closer to those observed in full Oldroyd–B simulations. The term is treated explicitly so as not to change the discrete energy law established for the unmodified scheme, and the factor $1-\gamma<1$ introduces a small net damping that prevents unbounded growth of the polymeric stretch.

We take $\mu = 1$ throughout and, unless otherwise specified, all examples are conducted in two spatial dimensions using unstructured Delaunay triangular meshes. The linear system at each time step is solved with a direct solver.

7.1. Convergence to a smooth solution on a uniform mesh. We first verify the accuracy of the spatial discretisation by studying the error with respect to the manufactured solution

$$(7.1) \quad \boldsymbol{u}(\boldsymbol{x},t) = (1,1)^{\mathsf{T}} + \sin\left(\frac{\pi t}{2}\right) \left(-\cos\left(\pi x\right)\sin\left(\pi y\right), \sin\left(\pi x\right)\cos\left(\pi y\right)\right)^{\mathsf{T}}, \quad \boldsymbol{b}(\boldsymbol{x},t) = \sin\left(\frac{\pi t}{2}\right) \left(-x,y\right)^{\mathsf{T}},$$

(7.2)
$$p(\boldsymbol{x},t) = \sin\left(\frac{\pi t}{2}\right)(x+y-1), \qquad r(\boldsymbol{x},t) = 0,$$

which yields divergence-free fields \boldsymbol{u} and \boldsymbol{b} . The spatial domain is the unit square and the final time is T=1. We take Re = Wi = 1 and $\beta = 1/2$. The flow is initialised with $\boldsymbol{u}_0 = \boldsymbol{0}$ and $\boldsymbol{b}_0 = (1,1)^{\mathsf{T}}$. We take the interior penalty parameter $\sigma_i = 10$ and $\sigma_b = 10^5$.

For elements of polynomial degree k = 1, 2, the discrete problem (6.1) is solved, with appropriate additional forcing terms, on a sequence of uniformly refined meshes with mesh parameters $h^{-1} = 4, 8, 16, 32$. The time step is coupled to the mesh as $\tau = h^{k+1}$. The resulting errors in \boldsymbol{u}_h and \boldsymbol{b}_h are measured in the norms

(7.3)
$$\|\boldsymbol{w}\|_{\mathcal{U}}^{2} := \|\boldsymbol{w}\|_{L^{\infty}(L^{2}(\Omega))}^{2} + \frac{\beta}{\operatorname{Re}} \|\nabla \boldsymbol{w}\|_{L^{2}(L^{2}(\Omega))}^{2},$$

(7.4)
$$\|\boldsymbol{w}\|_{\mathcal{B}}^{2} := \|\boldsymbol{w}\|_{L^{\infty}(L^{2}(\Omega))}^{2} + \frac{1-\beta}{\operatorname{Wi}^{2}} \|\boldsymbol{w}\|_{L^{2}(L^{2}(\Omega))}^{2},$$

and are plotted in Figure 1.

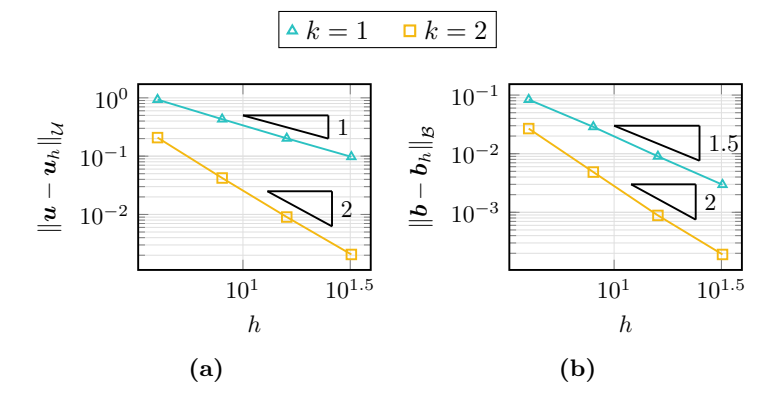


Fig. 1. Calculated errors for (a) u_h and (b) b_h , using finite elements of degree k = 1, 2, for the manufactured solution test of Section 7.1.

The results demonstrate convergence at a rate $\mathcal{O}\left(h^k\right)$ for $\|\boldsymbol{u}-\boldsymbol{u}_h\|_{\mathcal{U}}^2$, and at a rate between $\mathcal{O}\left(h^k\right)$ and $\mathcal{O}\left(h^{k+1}\right)$ for $\|\boldsymbol{b}-\boldsymbol{b}_h\|_{\mathcal{B}}^2$. This rate is expected to depend on the parameter choices. For instance, we have chosen $\beta=1/2$ to give a balance of inertial and elastic dynamics. Moving towards a purely elastic regime as $\beta\to 0$, or towards Newtonian flow as $\beta\to 1$, changes the character of the problem and hence its convergence properties.

7.2. Flow inside a lid-driven cavity. In the first physically motivated experiment we consider the lid-driven cavity problem, in which an initially stationary fluid is forced into motion by the movement of the upper boundary of a rectangular domain. In the context of viscoelastic fluids this problem has been widely studied, see for example [41, 5] and the references therein. It is a challenging test case due to the emergence of a boundary layer along the moving boundary, particularly near the corners, where large polymeric stresses accumulate and can trigger instabilities.

A diagram of the problem setup is shown in Figure 2. We solve (6.1) on the unit square with polynomial degree k=1, time step $\tau=3\times 10^{-3}$ and final time T=30. To resolve the boundary layer at the top of the cavity we employ a graded mesh (341,622 total degrees of freedom), with increased resolution towards the upper edge and especially near the upper corners. The smallest and largest element diameters are $h_K \approx 3\times 10^{-3}$ and $h_K \approx 10^{-2}$, respectively. We take the interior penalty parameter $\sigma_{\rm i}=10^2$ and $\sigma_{\rm b}=10^3$. We simulate creeping flow by choosing Re = 10^{-2} , and consider two Weissenberg regimes, Wi = 1/2 and Wi = 1. Unless otherwise stated we take $\beta=1/2$.

Along the top moving boundary Γ_D we prescribe $\boldsymbol{u} = (u_D, 0)^{\mathsf{T}}$, where

(7.5)
$$u_D(x,t) = 8(1 + \tanh 8(2t - 1/2)) x^2 (1 - x)^2,$$

and on the remaining boundary Γ_0 we impose no-slip and no-penetration conditions $\mathbf{u} = \mathbf{0}$. The initial conditions are $\mathbf{u}_0 = \mathbf{0}$ and $\mathbf{b}_0 = (1,0)^{\mathsf{T}}$. Representative snapshots of the resulting velocity field and polymeric

vector field (interpreted as the principal stretch direction) for Wi = 1/2 and Wi = 1 are shown in Figures 3 and 4, respectively. The centre of rotation for a Newtonian cavity flow is indicated for reference.

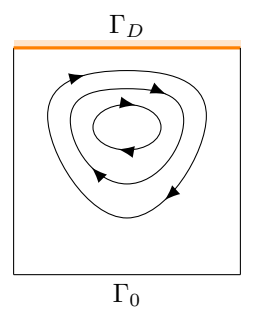


Fig. 2. The lid-driven cavity problem, in which an initially stationary fluid is forced into motion by the movement of the upper boundary $\Gamma_{\boldsymbol{u}}$ of a rectangular domain. The remaining boundary Γ_0 is fixed.

Without the inclusion of the extra forcing term we observe large spiral-like structures in the profile of b_h , which can be interpreted as a visualisation of polymer chains within the fluid. They decrease in magnitude but become longer and more pronounced as time evolves. The relaxation term ultimately dominates the stress generated at the lid and b_h is driven towards zero. Consequently, there is little-to-no visible viscoelastic influence on u_h . In particular, we do not observe the upward-left shift of the centre of fluid rotation (cf. Figure 2 in [5]), which is characteristic of viscoelastic flows in lid-driven cavities. We also highlight the rapid changes in the direction of b_h between neighbouring "spiral arms". At these sharp interfaces it is necessary that $|b_h| < 1$, regardless of the overall magnitude of the profile, indicating local polymer contraction and thus violating the assumption of a strongly elongated regime.

With the extra forcing term included, stress generated at the lid is sustained into the bulk and more complex flow patterns emerge. Similar rapid transitions in the direction of \boldsymbol{b}_h are observed, and their influence is clearly visible in the velocity field. The centre of fluid rotation moves upwards and left, although this is a transient effect and the velocity profile continues to adjust in response to the unsteady stress. Although the magnitude of \boldsymbol{b}_h is generally slightly larger in the Wi = 1 case (with a maximum of ≈ 24 compared to ≈ 21 when Wi = 1/2), the impact on the velocity is more pronounced in the smaller Weissenberg regime. This is consistent with the structure of the coupling term $(1-\beta)\text{Wi}^{-1}(\boldsymbol{b}\cdot\nabla)\boldsymbol{b}$ in (3.15): both the prefactor Wi⁻¹ and the spatial gradients of \boldsymbol{b}_h determine the effective forcing on the momentum equation, and in these simulations their combined effect is stronger at Wi = 1/2 despite the slightly larger peak values of $|\boldsymbol{b}_h|$ at Wi = 1. The recirculating flow may also play a role: opposing directions in the principal stress vector can promote local polymer contraction and thereby limit the growth of stress.

In Figure 5 we plot the evolution of the quantity

(7.6)
$$E_h^{\dagger}(t^n) := E_h(t^n) - E_h(t^{n-1}) + \tau \int_{\partial\Omega} \left(\operatorname{Re} \boldsymbol{u}_h \otimes \boldsymbol{u}_h : \boldsymbol{u}_h \otimes \boldsymbol{n} + p_h \boldsymbol{n} \cdot \boldsymbol{u}_h - 2\beta \boldsymbol{\varepsilon}(\boldsymbol{u}_h) : \boldsymbol{u}_h \otimes \boldsymbol{n} + \boldsymbol{u}_h \otimes \boldsymbol{b}_h : \boldsymbol{b}_h \otimes \boldsymbol{n} \right) ds,$$

which represents the instantaneous change of a modified energy that includes boundary contributions (a quantity that will also be relevant in the subsequent numerical experiments). The decay of the solution without the extra term towards a steady state, and the non-steady behaviour of the solution with the extra term, are both visible in the profiles of E_h^{\dagger} . In all cases E_h^{\dagger} remains non-positive, demonstrating energy decay consistent with an appropriately modified version of Theorem 6.3.

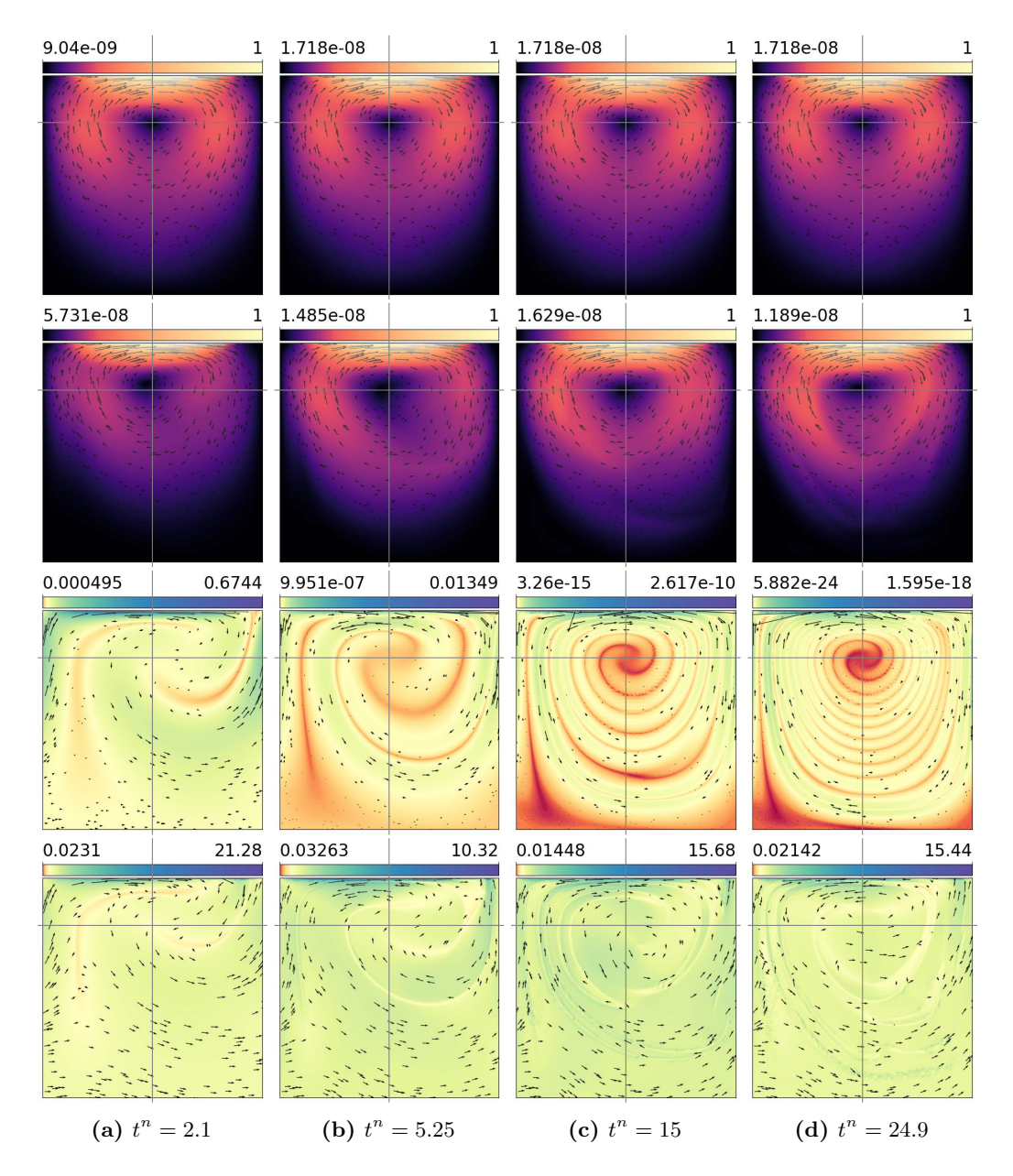


Fig. 3. Snapshots of u_h and b_h from the lid-driven cavity experiment in Section 7.2, with Wi = 1/2. The top and second rows show u_h without and with the extra forcing term, respectively, and the third and bottom rows show b_h without and with the extra forcing term, respectively. We draw particular attention to the logarithmic colour scales on each plot, which are used due to the nature of the boundary layer that arises along the top of the domain.

7.3. Flow through a pipe with a cavity. The second physically-motivated experiment is a natural extension of the lid-driven cavity, featuring flow through a pipe with a large cavity along one side. Modelling this situation is of practical interest for investigating the effects of elastic turbulence, which could be used to clear debris or other unwanted particles from the cavity region if introduced in an appropriate manner. Reentrant corners present a challenge to stability through flow separation and the influence on b of the gradient of the fluid velocity, which can become very large in the vicinity of the reentrant corner. Analytical results indicate that the velocity vanishes and the stress becomes singular at these points [27].

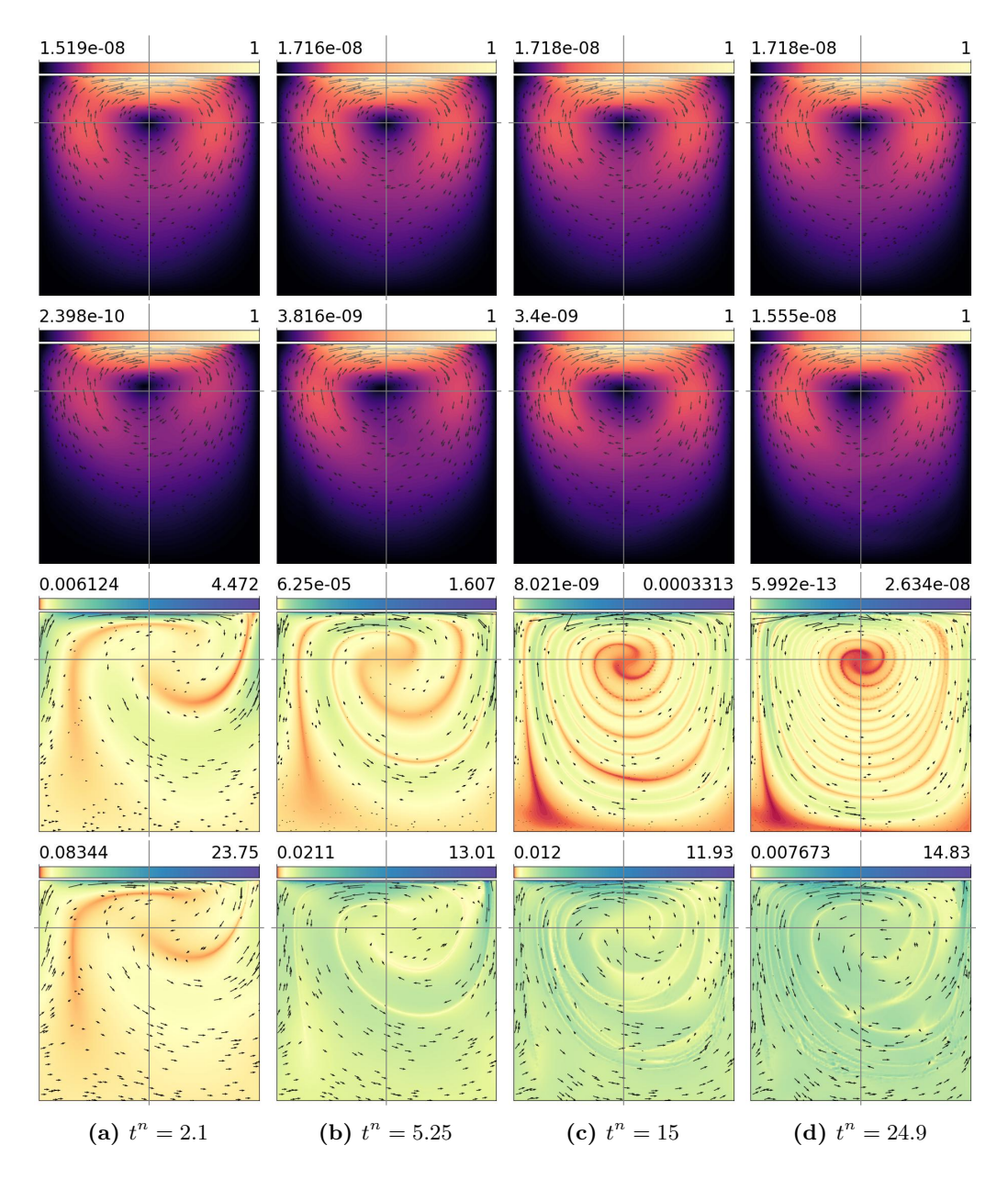


Fig. 4. Snapshots of u_h and b_h from the lid-driven cavity experiment in Section 7.2, with Wi = 1. The top and second rows show u_h without and with the extra forcing term, respectively, and the third and bottom rows show b_h without and with the extra forcing term, respectively. We draw particular attention to the logarithmic colour scales on each plot, which are used due to the nature of the boundary layer that arises along the top of the domain.

A sketch of the problem setup is shown in Figure 6, where we take $H_1 = H_2 = 1$, $L_1 = 6$, and $L_2 = 1.5$. The length of the pipe L_1 is taken greater than the other dimensions to allow the flow to fully develop before reaching the cavity. Taking T = 20 and $\tau = 5 \times 10^{-2}$, we solve (6.1) using polynomial degree k = 1 on a triangulation of the problem domain with increased resolution close to the boundary (139,341 total degrees of freedom). The mesh is particularly refined ($h_K \approx 2 \times 10^{-3}$) around the reentrant corners either side of the cavity, and the maximum mesh size is $h_K \approx 6 \times 10^{-2}$. We take $\sigma_i = 150$ and $\sigma_b = 10^6$. To simulate a creeping flow of a viscoelastic fluid, the problem parameter values are fixed as Re = 5×10^{-2} , Wi = 1,

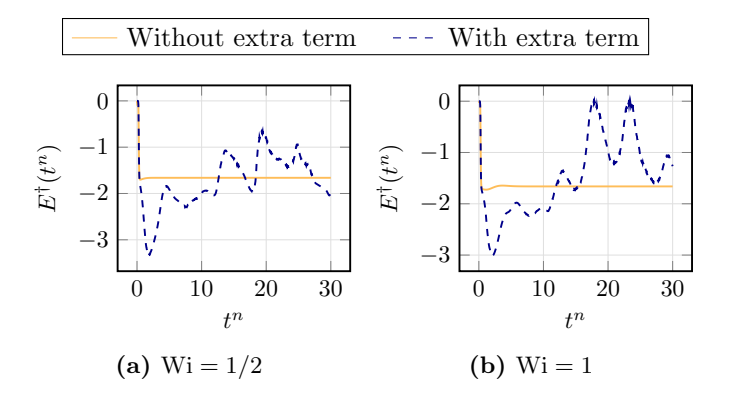


Fig. 5. Plots of the instantaneous rate of change of the modified energy (7.6) in the liddriven cavity experiments of Section 7.2. We emphasise that all values remain negative after initial time, and apparent contradictions are only plotting artifacts.

and we examine three polymer-to-solvent ratios: $\beta = 0.9$, $\beta = 0.5$, $\beta = 0.1$. The velocity is prescribed as parabolic on the inflow Γ_- as $\mathbf{u} = (u_-, 0)^{\mathsf{T}}$, with

(7.7)
$$u_{-}(y,t) = \frac{4}{H_{1}^{2}} \tanh 40ty(H_{1} - y).$$

On the outflow Γ_+ , the natural boundary condition $-\nabla u \cdot n + pn = 0$ reduces to the do-nothing condition $\nabla u \cdot n = 0$ by fixing p = 0. On the remaining boundaries, denoted Γ_0 , we set the no-slip, no-penetration condition u = 0. We set $b = (1,0)^{\mathsf{T}}$ on the inflow boundary. The initial conditions are the same as in Section 7.2, with $u_0 = 0$ and $b_0 = (1,0)^{\mathsf{T}}$. We note that, due to the do-nothing condition on the outflow, the pressure is fully-determined so no mean-zero condition is required.

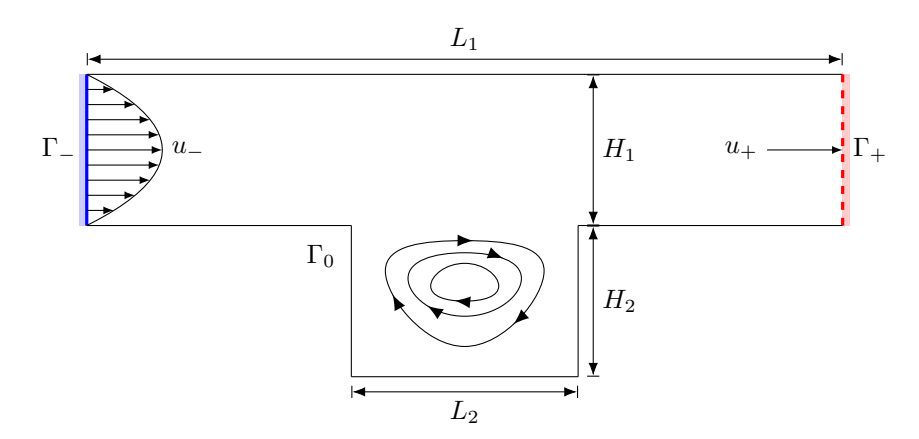


Fig. 6. A sketch of the cavity flow problem setup in Section 7.3. The blue line represents the fluid inflow Γ_{-} , and the red dashed line represents the outflow Γ_{+} . The remaining boundary Γ_{0} represents fixed walls.

The resulting polymeric stress and velocity profiles are depicted at final time without the extra term in Figure 7 and with the extra term included in Figure 8. In both cases it can be seen that the maximum stress attained decreases as β does, whereas the maximum velocity increases and becomes more affected by the viscoelastic properties of the fluid. Without the extra term present, the stress set at the inflow quickly dies away towards zero as the flow progresses into the domain. Consequently, the velocity profile in these cases remains very similar to that of a Newtonian fluid (e.g. symmetric vortices in the cavity), with only minor deviations visible in the $\beta = 0.1$ case. On the other hand, when the extra term is included the stress

is preserved into the bulk and the reentrant corners at the top of the cavity generate large local stress. This feeds back into the velocity profile, and it can be seen that as β decreases, the overall velocity in the cavity decreases and a single centre of fluid rotation emerges, breaking the previously-observed symmetry.

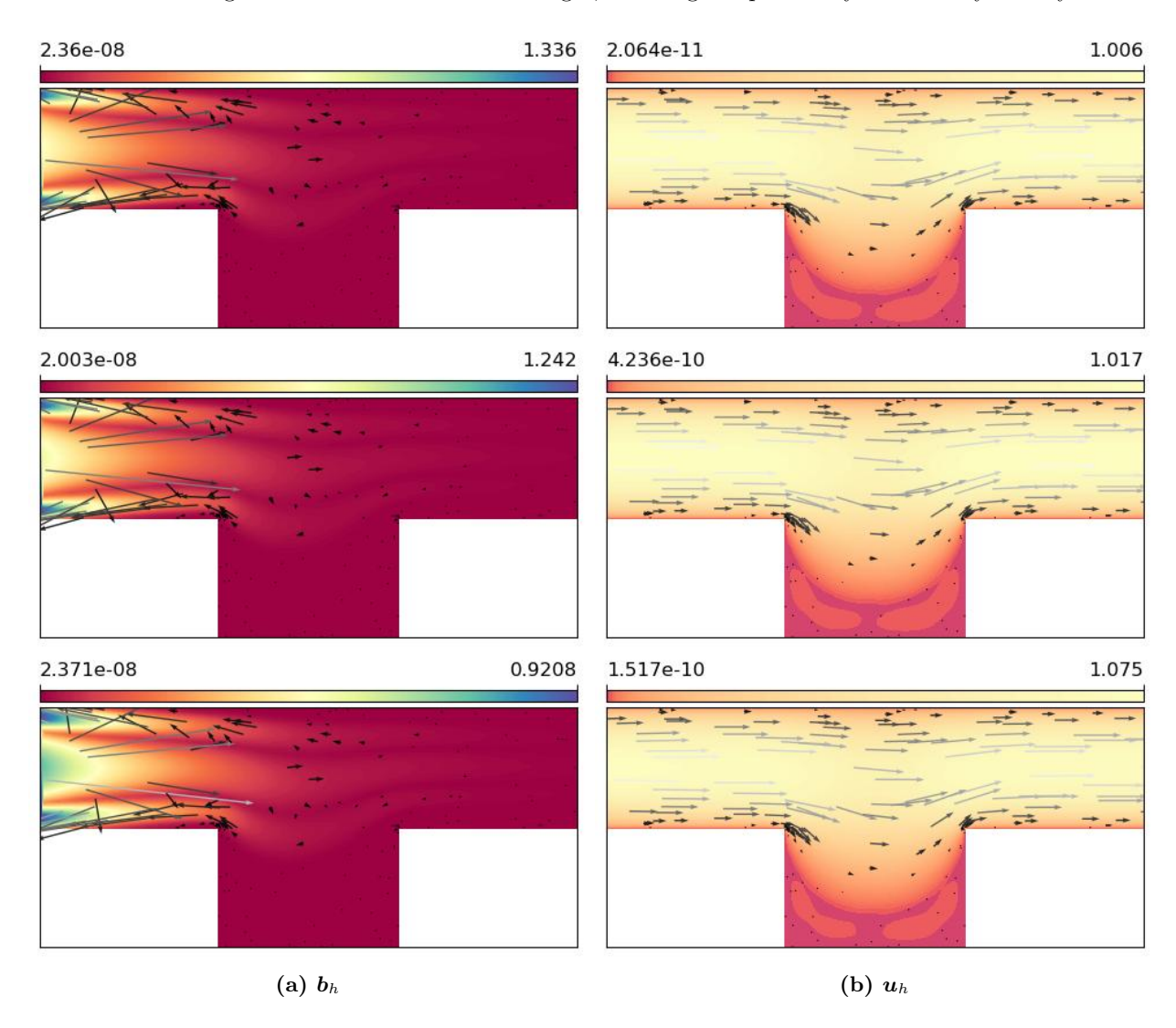


Fig. 7. Snapshots at the final time of b_h and u_h with (top) $\beta = 0.9$, (middle) $\beta = 0.5$, and (bottom) $\beta = 0.1$ from the pipe-with-cavity experiments in Section 7.3 without the extra term included. The velocity plots are coloured on a logarithmic scale to emphasise the flow structures present in the cavity.

We plot the instantaneous energy change for this problem in Figure 9. The magnitude of the energy change decreases with β , since the velocity dissipation term loses significance, emphasising the viscoelasticity of the fluid. In all cases the energy is monotonically decreasing.

7.4. **4:1 planar contraction flows.** Another class of problems typically used to benchmark numerical methods for viscoelastic flows are planar contraction flows, in which a fluid flows through a two-dimensional channel featuring a sudden width constriction. Physical experiments highlight the wide range of flow dynamics that can be observed by slight adjustments to the geometry or fluid properties [21].

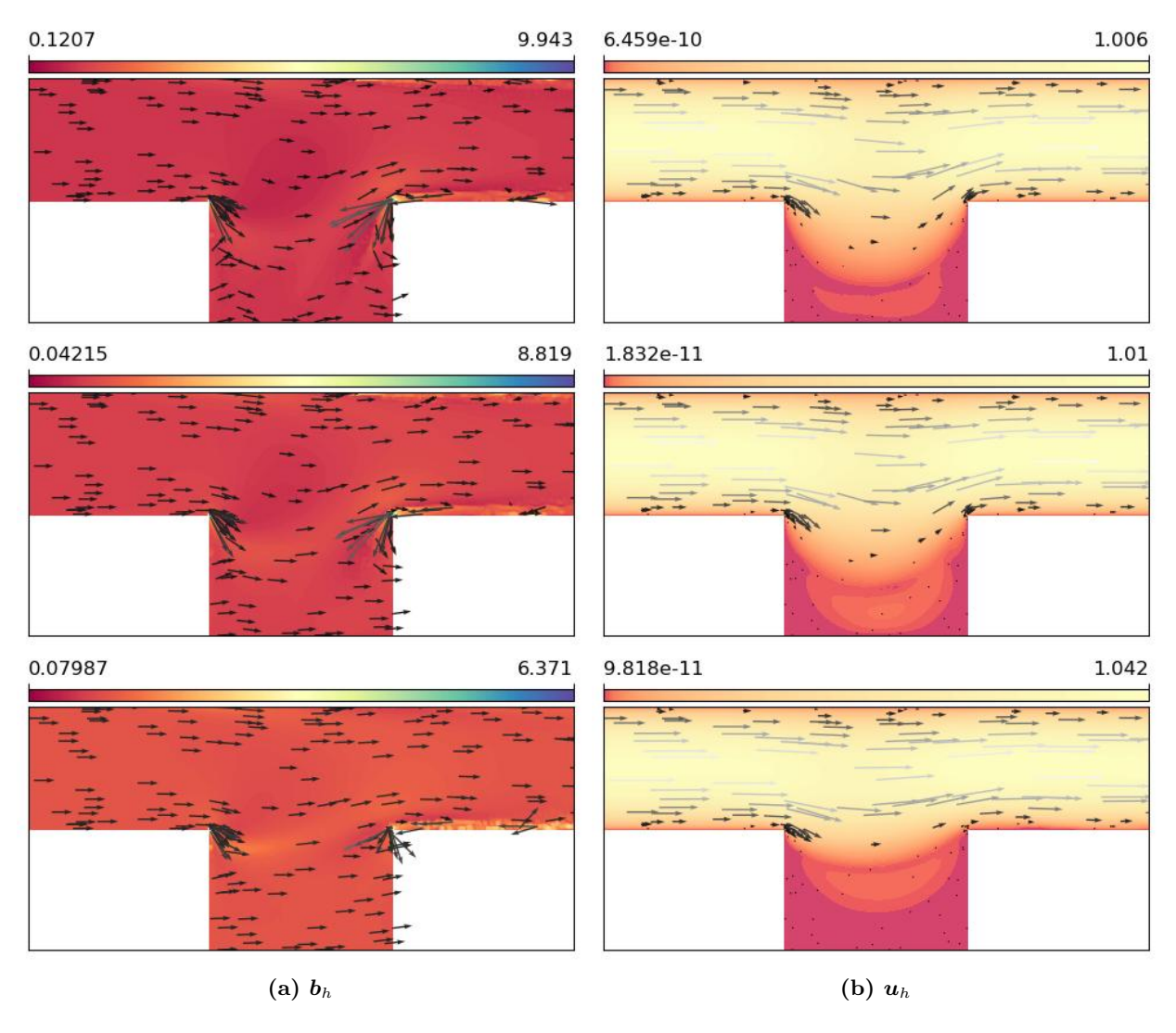


Fig. 8. Snapshots at the final time of b_h and u_h with (top) $\beta = 0.9$, (middle) $\beta = 0.5$, and (bottom) $\beta = 0.1$ from the pipe-with-cavity experiments in Section 7.3 with the extra term included. The velocity plots are coloured on a logarithmic scale to emphasise the flow structures present in the cavity.

A sketch of the problem setup can be seen in Figure 10, where we take a pre-contraction channel length of $L_1 = 2$ and width of $H_1 = 1$ and a post-contraction channel length of $L_2 = 1$ and width of $H_2 = 0.25$. This gives a 4:1 contration ratio (H_1/H_2) , which is a common choice in the literature. However, the ratio can have important influence, and some flow features are only observed with certain setups [1].

Fixing the final time as T=20 and the time step size as $\tau=10^{-3}$, we solve (6.1), with polynomial degree k=1, on a triangulation (56,876 total degrees of freedom) of the spatial domain. The triangulation features increased resolution around the boundaries and especially the reentrant corners, which we regularise by rounding to have radius 0.02 and about which $h_K \approx 10^{-3}$. We take $\sigma_i = 300$ and $\sigma_b = 10^6$. Taking Re = 10^{-2} and $\beta = 0.9$, we consider three Weissenberg number regimes: Wi = 1.4, Wi = 1.5, Wi = 1.6. As in the previous pipe-with-cavity experiment, the velocity is prescribed on the inflow boundary Γ_- as $\boldsymbol{u} = (u_-, 0)^{\mathsf{T}}$, where u_- is defined in (7.7), and the do-nothing condition $\nabla \boldsymbol{u} \cdot \boldsymbol{n} = \boldsymbol{0}$ is satisfied on the outflow boundary Γ_+ by fixing p=0. The remaining boundaries, denoted Γ_0 , feature the no-slip, nopenetration condition $\boldsymbol{u} = \boldsymbol{0}$. We set $\boldsymbol{b} = (2,0)^{\mathsf{T}}$ on the inflow boundary, and the do-nothing condition for

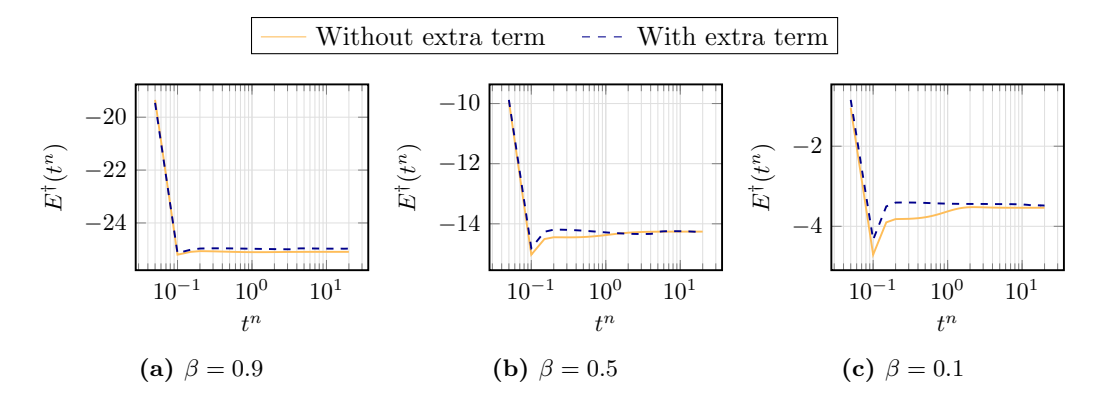


Fig. 9. Plots of the instantaneous rate of change of the modified energy (7.6) in the pipe-with-cavity experiments of Section 7.3.

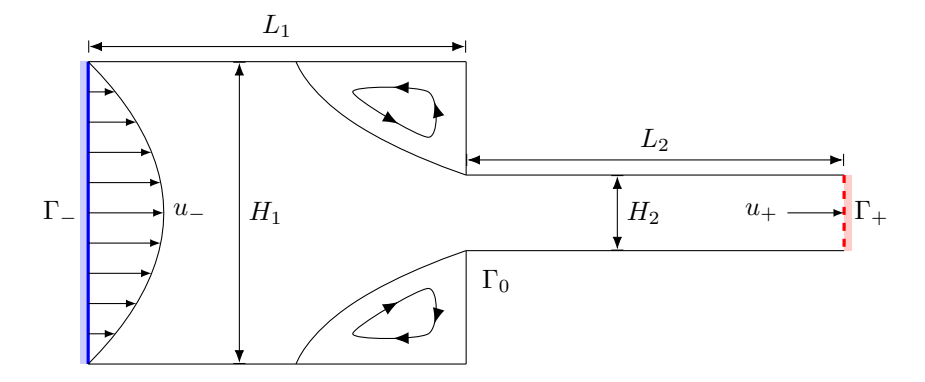


Fig. 10. A sketch of the 4:1 contraction flow problem setup in Section 7.4. The blue line represents the fluid inflow Γ_{-} , and the red dashed line represents the outflow Γ_{+} . The remaining boundary Γ_{0} represents fixed walls.

 \boldsymbol{b} is satisfied by fixing r=0 on the remaining boundary. The initial conditions are given as $\boldsymbol{u}_0=\boldsymbol{0}$ and $\boldsymbol{b}_0=(2,0)^{\mathsf{T}}$. Again, due to due to setting the pressure on the outflow, it is fully-determined and no mean-zero condition is required.

Snapshots of the principal polymeric stress and velocity profiles at $t^n=5$ are shown without the extra term in Figure 11 and with the extra term in Figure 12. This plotting time is chosen to exemplify the differences between the flows for different Weissenberg numbers. In all cases stress is advected along with the flow and builds up around the reentrant corners. As in the previous numerical experiments, without the extra term the bulk stress decays to zero, but with the extra term two different effects occur after sufficient stress has accumulated. As Wi increases vortices appear in the top and bottom corners in line with the contraction, where the magnitude of the velocity is small, and they grow in strength. Then, in the Wi = 1.6 case, the flow develops oscillations further upstream of the contraction, which can be observed in both the stress and velocity profiles. Both of these behaviours are in line with results from the literature, with first corner vortices appearing for Weissenberg numbers above a certain value and then oscillations at even higher values.

The instantaneous energy change for the 4:1 contraction flow experiments are shown in Figure 13, where the monotonic energy decrease is demonstrated in all cases. Although the changes are minor between each of the Weissenberg number cases, the impact can be seen as a slight increase as Wi grows in the experiments including the extra term, indicating that the problem becomes less dissipative.

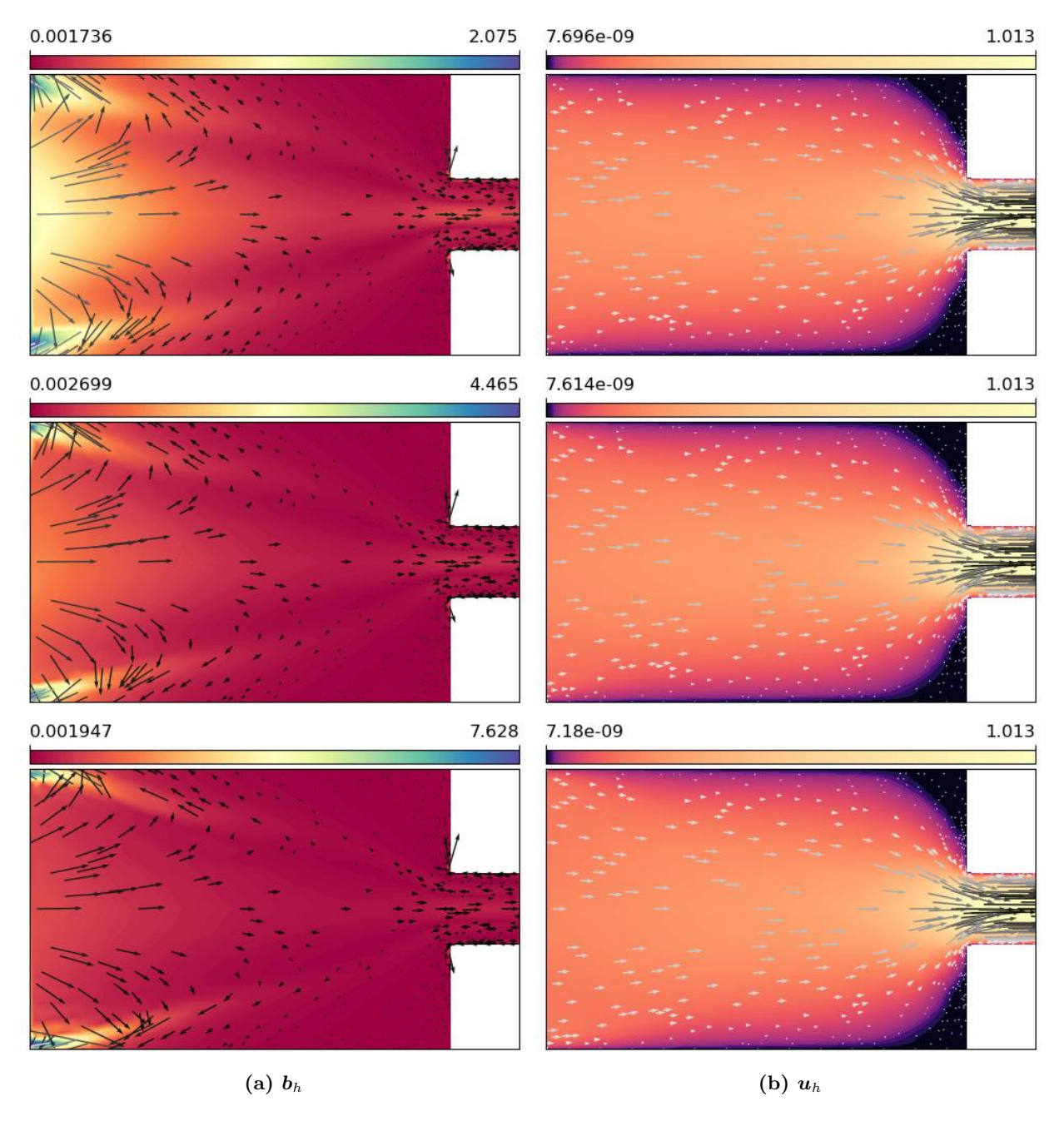


Fig. 11. Snapshots at $t^n = 5$ of \boldsymbol{b}_h and \boldsymbol{u}_h with (top) Wi = 1.4, (middle) Wi = 1.5, and (bottom) Wi = 1.6 from the 4:1 contraction experiments in Section 7.4 without the extra term included. The plots are coloured on a logarithmic scale to emphasise the structures present.

8. Conclusions

In this work, we developed a finite element framework for a uniaxial reduction of the Oldroyd-B model. We derived spatially semidiscrete and fully discrete formulations, ensuring compatibility with the underlying PDE stability framework. Existence and uniqueness of solutions were shown for the spatially semidiscrete and fully discrete problems.

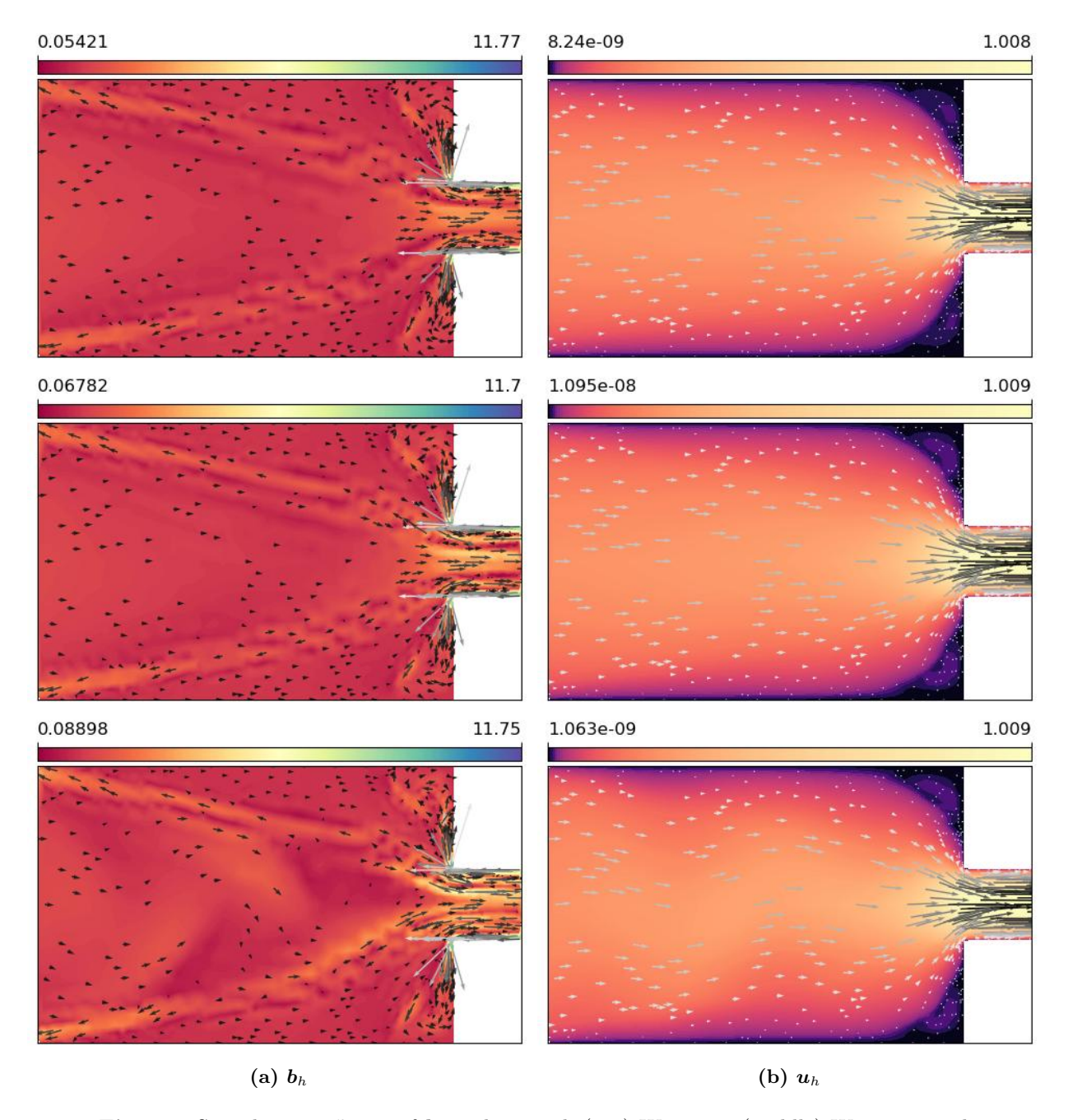


Fig. 12. Snapshots at $t^n = 5$ of \boldsymbol{b}_h and \boldsymbol{u}_h with (top) Wi = 1.4, (middle) Wi = 1.5, and (bottom) Wi = 1.6 from the 4:1 contraction experiments in Section 7.4 with the extra term included. The plots are coloured on a logarithmic scale to emphasise the structures present.

Numerical experiments validated the approach on benchmark problems. These results confirmed the robustness of the method for handling high Weissenberg numbers and resolving sharp stress gradients. Despite the simplifications introduced by the uniaxial reduction, key features of viscoelastic flow dynamics, such as elastic effects and flow instabilities, were captured.

Future research could focus on extending the framework to handle multi-component polymeric flows or incorporating additional physical effects, such as temperature-dependence or shear-thinning behaviour.

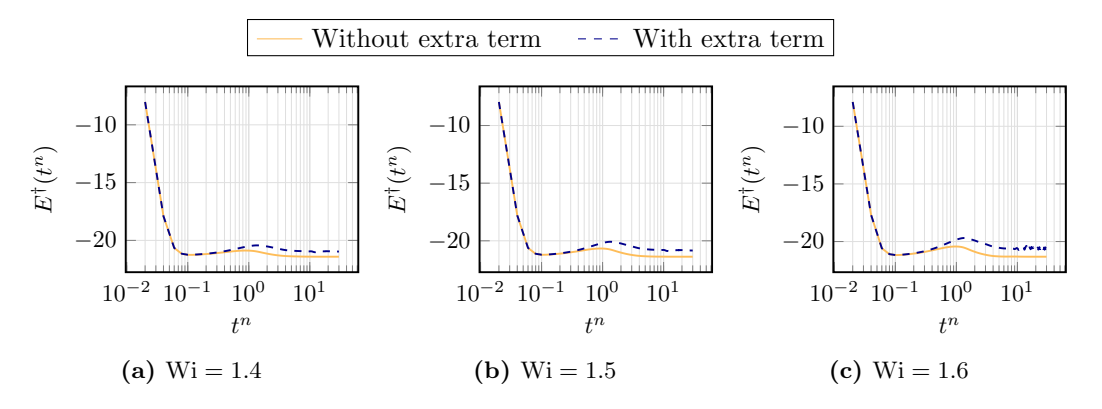


Fig. 13. Plots of the instantaneous rate of change of the modified energy (7.6) in the 4:1 planar contraction flow experiments of Section 7.4.

Investigating the limitations of the uniaxial model, particularly in regimes where isotropic stress components are significant, is another direction.

References

- [1] M. A. Alves, P. J. Oliveira, and F. T. Pinho. "On the effect of contraction ratio in viscoelastic flow through abrupt contractions". In: *Journal of non-newtonian fluid mechanics* 122.1-3 (2004), pp. 117–130.
- [2] D. N. Arnold, R. S. Falk, and R. Winther. "Finite element exterior calculus, homological techniques, and applications". In: *Acta numerica* 15 (2006), pp. 1–155.
- [3] D. N. Arnold, F. Brezzi, B. Cockburn, and L. D. Marini. "Unified Analysis of Discontinuous Galerkin Methods for Elliptic Problems". In: SIAM Journal on Numerical Analysis 39.5 (2002), pp. 1749–1779. DOI: 10.1137/S0036142901384162.
- [4] U. M. Ascher, S. J. Ruuth, and B. T. Wetton. "Implicit-explicit methods for time-dependent partial differential equations". In: SIAM Journal on Numerical Analysis 32.3 (1995), pp. 797–823.
- [5] B. S. Ashby and T. Pryer. "Discretisation of an Oldroyd-B viscoelastic fluid flow using a Lie derivative formulation". In: *Advances in Computational Mathematics* 51.1 (2025), p. 1.
- [6] J. W. Barrett, C. Schwab, and E. Süli. "Existence of global weak solutions for some polymeric flow models". In: Mathematical models and methods in applied sciences 15.06 (2005), pp. 939–983.
- [7] C. Bernardi, V. Girault, F. Hecht, P.-A. Raviart, and B. Rivière. *Mathematics and Finite Element Discretizations of Incompressible Navier-Stokes Flows.* Philadelphia, PA: Society for Industrial and Applied Mathematics, 2024. DOI: 10.1137/1.9781611978124. eprint: https://epubs.siam.org/doi/pdf/10.1137/1.9781611978124. URL: https://epubs.siam.org/doi/abs/10.1137/1.9781611978124.
- [8] R. B. Bird, R. C. Armstrong, and O. Hassager. "Dynamics of polymeric liquids. Vol. 1: Fluid mechanics". In: (1987).
- [9] D. Boffi, F. Brezzi, M. Fortin, et al. Mixed finite element methods and applications. Vol. 44. Springer, 2013.
- [10] D. Boger. "Viscoelastic flows through contractions". In: Annual review of fluid mechanics 19.1 (1987), pp. 157–182.
- [11] S. Boyaval. "Lid-driven-cavity simulations of Oldroyd-B models using free-energy-dissipative schemes". In: Numerical Mathematics and Advanced Applications 2009: Proceedings of ENUMATH 2009, the 8th European Conference on Numerical Mathematics and Advanced Applications, Uppsala, July 2009. Springer. 2010, pp. 191–198.
- [12] S. Boyaval, T. Lelièvre, and C. Mangoubi. "Free-energy-dissipative schemes for the Oldroyd-B model". In: ESAIM: Mathematical Modelling and Numerical Analysis 43.3 (2009), pp. 523–561.

- [13] E. Burman and M. Fernándes. "Continuous interior penalty finite element method for the time-dependent Navier-Stokes equations: space discretization and convergence". In: *Numer. Math.* 107 (2007), pp. 39–77.
- [14] J. Chen, D. Han, B. Yu, D. Sun, and J. Wei. "A POD-Galerkin reduced-order model for isotropic viscoelastic turbulent flow". In: *International Communications in Heat and Mass Transfer* 84 (2017), pp. 121–133.
- [15] M. Chetry, D. Borzacchiello, G. D'Avino, and L. R. Da Silva. "Comparing different stabilization strategies for reduced order modeling of viscoelastic fluid flow problems". In: *Computers & Fluids* 265 (2023), p. 106013.
- [16] B. Cockburn. "An introduction to the discontinuous Galerkin method for convection-dominated problems". In: Advanced Numerical Approximation of Nonlinear Hyperbolic Equations: Lectures given at the 2nd Session of the Centro Internazionale Matematico Estivo (CIME) held in Cetraro, Italy, June 23–28, 1997. Springer, 2006, pp. 150–268.
- [17] B. Cockburn, G. Kanschat, and D. Schotzau. "A locally conservative LDG method for the incompressible Navier-Stokes equations". In: *Math. Comp.* 74.251 (2005), pp. 1067–1095. ISSN: 0025-5718,1088-6842. DOI: 10.1090/S0025-5718-04-01718-1. URL: https://doi.org/10.1090/S0025-5718-04-01718-1.
- [18] R. Comminal, J. Spangenberg, and J. H. Hattel. "Robust simulations of viscoelastic flows at high Weissenberg numbers with the streamfunction/log-conformation formulation". In: Journal of Non-Newtonian Fluid Mechanics 223 (2015), pp. 37–61.
- [19] M. J. Crochet, A. R. Davies, and K. Walters. Numerical simulation of non-Newtonian flow. Vol. 1. Elsevier, 2012.
- [20] J. M. Dealy. "Weissenberg and Deborah numbers—their definition and use". In: *Rheol. Bull* 79.2 (2010), pp. 14–18.
- [21] R. Evans and K. Walters. "Flow characteristics associated with abrupt changes in geometry in the case of highly elastic liquids". In: *Journal of Non-Newtonian Fluid Mechanics* 20 (1986), pp. 11–29.
- [22] R. Fattal and R. Kupferman. "Constitutive laws for the matrix-logarithm of the conformation tensor". In: Journal of Non-Newtonian Fluid Mechanics 123.2-3 (2004), pp. 281–285.
- [23] R. Fattal and R. Kupferman. "Time-dependent simulation of viscoelastic flows at high Weissenberg number using the log-conformation representation". In: *Journal of Non-Newtonian Fluid Mechanics* 126.1 (2005), pp. 23–37.
- [24] A. Fouxon and V. Lebedev. "Spectra of turbulence in dilute polymer solutions". In: *Physics of Fluids* 15.7 (2003), pp. 2060–2072.
- [25] R. Guénette and M. Fortin. "A new mixed finite element method for computing viscoelastic flows". In: Journal of non-newtonian fluid mechanics 60.1 (1995), pp. 27–52.
- [26] P. Hansbo and M. G. Larson. "Discontinuous Galerkin methods for incompressible and nearly incompressible elasticity by Nitsche's method". In: Computer Methods in Applied Mechanics and Engineering 191.17 (2002), pp. 1895–1908. ISSN: 0045-7825. DOI: https://doi.org/10.1016/S0045-7825(01) 00358-9. URL: https://www.sciencedirect.com/science/article/pii/S0045782501003589.
- [27] E. Hinch. "The flow of an Oldroyd fluid around a sharp corner". In: *Journal of Non-Newtonian Fluid Mechanics* 50.2-3 (1993), pp. 161–171.
- [28] J. Hinch and O. Harlen. "Oldroyd B, and not A?" In: Journal of Non-Newtonian Fluid Mechanics 298 (2021), p. 104668.
- [29] D. Hu and T. Leliévre. "New entropy estimates for the Oldroyd-B model and related models". In: (2007).
- [30] T. J. Hughes, L. P. Franca, and M. Mallet. "A new finite element formulation for computational fluid dynamics: VI. Convergence analysis of the generalized SUPG formulation for linear time-dependent multidimensional advective-diffusive systems". In: Computer Methods in Applied Mechanics and Engineering 63.1 (1987), pp. 97–112.
- [31] M. A. Hulsen, R. Fattal, and R. Kupferman. "Flow of viscoelastic fluids past a cylinder at high Weissenberg number: stabilized simulations using matrix logarithms". In: Journal of Non-Newtonian Fluid Mechanics 127.1 (2005), pp. 27–39.

- [32] A. Jafari, A. Chitsaz, R. Nouri, and T. N. Phillips. "Property preserving reformulation of constitutive laws for the conformation tensor: A. Jafari et al." In: *Theoretical and Computational Fluid Dynamics* 32.6 (2018), pp. 789–803.
- [33] R. Keunings. "On the high Weissenberg number problem". In: Journal of Non-Newtonian Fluid Mechanics 20 (1986), pp. 209–226.
- [34] P. Lions and N. Masmoudi. "Global solutions for some Oldroyd models of non-Newtonian flows". In: Chinese Annals of Mathematics 21.02 (2000), pp. 131–146.
- [35] A. Lozinski and R. G. Owens. "An energy estimate for the Oldroyd B model: theory and applications". In: *Journal of non-newtonian fluid mechanics* 112.2-3 (2003), pp. 161–176.
- [36] G. I. Ogilvie and M. R. Proctor. "On the relation between viscoelastic and magnetohydrodynamic flows and their instabilities". In: *Journal of Fluid Mechanics* 476 (2003), pp. 389–409.
- [37] M. S. Oliveira, P. J. Oliveira, F. T. Pinho, and M. A. Alves. "Effect of contraction ratio upon viscoelastic flow in contractions: The axisymmetric case". In: *Journal of Non-Newtonian Fluid Mechanics* 147.1-2 (2007), pp. 92–108.
- [38] R. G. Owens and T. N. Phillips. Computational rheology. World Scientific, 2002.
- [39] P. Pakdel and G. H. McKinley. "Cavity flows of elastic liquids: purely elastic instabilities". In: *Physics of Fluids* 10.5 (1998), pp. 1058–1070.
- [40] P. Pakdel, S. H. Spiegelberg, and G. H. McKinley. "Cavity flows of elastic liquids: two-dimensional flows". In: *Physics of Fluids* 9.11 (1997), pp. 3123–3140.
- [41] T.-W. Pan, J. Hao, and R. Glowinski. "On the simulation of a time-dependent cavity flow of an Oldroyd-B fluid". In: *International Journal for Numerical Methods in Fluids* 60.7 (2009), pp. 791–808.
- [42] W.-H. Zhang, J. Li, Q. Wang, Y. Ma, H.-N. Zhang, B. Yu, and F. Li. "Comparative study on numerical performances of log-conformation representation and standard conformation representation in the simulation of viscoelastic fluid turbulent drag-reducing channel flow". In: *Physics of Fluids* 33.2 (2021).

BEN S. ASHBY INSTITUTE FOR MATHEMATICAL INNOVATION, UNIVERSITY OF BATH, BATH BA2 7AY, UK bsa34@bath.ac.uk.

GABRIEL R. BARRENECHEA DEPARTMENT OF MATHEMATICS AND STATISTICS, UNIVERSITY OF STRATHCLYDE, 26 RICHMOND STREET, GLASGOW G1 1XK, UK, gabriel.barrenechea@strath.ac.uk.

ALEX LUKYANOV DEPARTMENT OF MATHEMATICS AND STATISTICS, UNIVERSITY OF READING, a.lukyanov@reading.ac.uk.

TRISTAN PRYER DEPARTMENT OF MATHEMATICAL SCIENCES, UNIVERSITY OF BATH, BATH BA2 7AY, UK tmp38@bath.ac.uk.

ALEX TRENAM THE MAXWELL INSTITUTE FOR MATHEMATICAL SCIENCES & MATHEMATICS-DRIVEN INNOVATION CENTRE, SCHOOL OF MATHEMATICAL AND COMPUTER SCIENCES, HERIOT-WATT UNIVERSITY, EDINBURGH, EH14 4AS, UK. A.Trenam@hw.ac.uk.